

A Spectroscopic Study of Supernova Remnants with the Infrared Space Observatory*

MATTHEW J. MILLARD,¹ ARAVIND P. RAVI,¹ JEONGHEE RHO,² AND SANGWOOK PARK¹

¹*Box 19059, Department of Physics, University of Texas at Arlington, Arlington, TX 76019*

²*SETI Institute, 189 N. Bernardo Ave, Suite 200, Mountain View, CA 94043, USA*

ABSTRACT

We present far-infrared (FIR) spectroscopy of supernova remnants (SNRs) based on the archival data of the Infrared Space Observatory (*ISO*) taken with the Long Wavelength Spectrometer (LWS). Our sample includes previously unpublished profiles of line and continuum spectra for 20 SNRs in the Galaxy and Magellanic Clouds. In several SNRs including G21.5–0.9, G29.7–0.3, the Crab Nebula, and G320.4–1.2, we find evidence for broad [O I], [O III], [N II], and [C II] lines with velocity dispersions up to a few 10^3 km s^{−1}, indicating that they are associated with high-velocity SN ejecta. Our detection of Doppler-broadened atomic emission lines and a bright FIR continuum hints at the presence of newly formed dust in SN ejecta. For G320.4–1.2, we present the first estimate of an ejecta-dust mass of 0.1 – 0.2 M_⊙, which spatially coincides with the broad line emission, by applying a blackbody model fit with components of the SNR and background emission. Our sample includes raster maps of 63, 145 μm [O I] and 158 μm [C II] lines toward SNRs Kes 79, CTB 109, and IC 443. Based on these line intensities, we suggest interacting shock types in these SNRs. Finally, we compare our LWS spectra of our sample SNRs with the spectra of several HII regions, and discuss their FIR line intensity ratios and continuum properties. Follow-up observations with modern instruments (e.g. *JWST* and *SOFIA*) with higher spatial and spectral resolution are encouraged for an extensive study of the SN ejecta and the SN dust.

Keywords: astrochemistry:oxygen – infrared:supernova remnants – dust:shock waves

1. INTRODUCTION

Supernovae (SNe) enrich the interstellar medium (ISM) by dispersing metal-rich ejecta created in the SN explosion into their surrounding environment. In the years following a CCSN (since Type Ia SNe have not been observed to form dust), the ejecta cools quickly as it expands, allowing chemical reactions to take place, which leads to the creation of molecules and dust grains in the ejecta (Todini & Ferrara 2001; Nozawa et al. 2003; Sarangi & Cherchneff 2015; Sluder et al. 2018). The elements comprising these grains, including Si and O, will likely remain locked in dust until they encounter a strong reverse shock created by the interaction of the blast wave and the ISM, or the shock wave from

the pulsar wind nebula (PWN). The ejecta are compressed and heated by the shock, causing ionization and destruction of the molecules and dust within. Once the ejecta cools to $\sim 10^2 - 10^3$ K, line emission from atomic fine-structure transitions is radiated in the far-infrared (FIR) band. These emission lines originate from a rapidly expanding shell of ejecta and therefore are broadened due to the Doppler effect. The radiation from the surviving dust grains shows a blackbody-like spectrum (the so-called “grey-body”), where the overall flux level depends on the total mass of the dust.

It has yet to be determined if SNe are major sources of dust in the Universe. The large quantity of dust observed in high-redshift galaxies (Bertoldi et al. 2003; Laporte et al. 2017; Isaak et al. 2002; Hirashita et al. 2017) raises the fundamental astrophysical question on the origin of dust in the Universe, because the timescales of dust formation in low-mass stellar winds are longer than the age of the Universe in that era. On the other hand, CC-SNe of massive stars may create dust on short timescales of \lesssim several 10^6 yr (Morgan & Edmunds 2003; Dwek & Arendt 2008), and thus are compelling candi-

Corresponding author: Matthew J. Millard
matthew.millard@mavs.uta.edu

*Based on observations with *ISO*, an ESA project with instruments funded by ESA Member States (especially the PI countries: France, Germany, the Netherlands and the United Kingdom) and with the participation of ISAS and NASA.

date sources for significant dust production in the early Universe.

The Long Wavelength Spectrometer (LWS; Clegg et al. 1996) on board the *Infrared Space Observatory* (*ISO*; Kessler et al. 1996) operated in the 43 – 196.8 μm band, making it an ideal instrument for measuring FIR atomic fine-structure lines and continuum emission from cool dust in SN ejecta. The *ISO* mission lasted from November 1995 to May 1998, utilizing a 60-cm diameter primary mirror cooled to 1.7 K with superfluid helium, and performed over 26,000 scientific observations during its run. *ISO* was an important tool for the diagnosis of the physics and chemistry of a wide range of astrophysical objects. For a comprehensive review of the achievements of *ISO*, see Cesarsky & Salama (2006). Although it had made significant contributions in the field of infrared astronomy, some archival *ISO* data sets have yet to be analyzed, including a substantial fraction of the supernova remnant (SNR) observations.

To make use of the unpublished archival *ISO* spectroscopic data, we probed the *ISO* data archive for LWS spectra of SNRs. In these spectra, we search for Doppler-broadened atomic fine-structure emission lines due to high-speed ejecta that are also coincident with bright continuum emission from dust. Based on these emission lines and underlying FIR continuum, we study the characteristics of the shocked gas and dust. We present the results of our FIR spectroscopic study of 18 CC-SNRs. We also present our FIR emission line profile measurements for two Type Ia SNRs (Kepler’s and Tycho’s SNRs) in this work. Although Type Ia SNe would unlikely contribute to the dust budget of the early Universe, our measurements of FIR fine-structure emission line profiles may be helpful to search for unshocked ejecta in these historical Type Ia SNRs (which is beyond the scope of this work). We investigate our sample by comparing [O I] and [C II] line strengths in several SNRs interacting with molecular clouds with various shock models. Finally, we present previously unpublished LWS data of HII regions to compare their emission line profiles and ratios with those for SNRs. We show that several FIR line flux ratios may be useful to differentiate SNRs from HII regions in future SNR searches.

2. OBSERVATIONS AND DATA

2.1. Sample Selection

We searched the *ISO* data archive for LWS observations of SNRs. We identified 31 instances of observations

where the data are unpublished, including 20 individual SNRs. Table 1 lists these observations. *ISO* LWS observations of SNRs that are not included in our sample are shown in Appendix A (Table A.1). For each observation in our sample, we selected the Highly Processed Data Products (HPDPs)¹ from the archive (Lloyd et al. 2003). We use the average values of the forward and reverse scans in our analysis. We also compare the unpublished LWS data from the HII regions W51, G159.6–18.5, and NGC 6334, and the planetary nebula (PN) NGC 6720, with the SNR spectra.

2.2. The LWS Spectra

The LWS consists of 10 subdetectors (SW1 – SW5 and LW1 – LW5), each covering a fraction of the total LWS wavelength range, 43 – 197 μm . These spectra are often “fractured” – the flux levels of some detectors do not match adjacent detectors by up to $\sim 10\%$. To align the flux levels between adjacent detectors, we scaled each subdetector spectrum based on the average flux of the overlapping wavebands such that the full broadband spectrum becomes continuous without any jump in flux density. This scaling negligibly affects the emission line profiles. However, the scaled overall flux level of the continuum may vary by up to a factor of ~ 2 . Since SNRs in our sample are diffuse emission sources, we applied the effective area correction for the extended sources (Gry et al. 2003) (Section 6). Application of the extended source correction causes the overall flux level of the spectrum to be reduced by up to 40%. In Figure 1, we show an example of the LWS spectrum before and after the flux scaling and application of extended source correction. Figures 2 – 24 show the resulting minimum broadband LWS spectrum of each SNR and HII region in our sample, along with the pointing position and aperture (80'' diameter) overlaid on an infrared image of the SNR from *Herschel*, *Spitzer*, or *WISE* observations. The line fluxes are listed in Table 2 and the changes in the fluxes between the minimum and maximum broadband spectra are less than 1%.

We found that some flux values in the LWS spectra have zero uncertainties. The wavelengths at which these zero flux uncertainties appear vary depending on the observation. Their origin is unclear, although they may originate from glitches in the detector photocurrent. In some cases, these fluxes were in regions of interest (at wavelengths corresponding to identified emission lines) in the LWS spectra. Since these values were consistent with the fluxes that have non-zero uncertainties, instead of removing them, we assigned the largest uncertainty value in the subdetector spectrum to these fluxes.

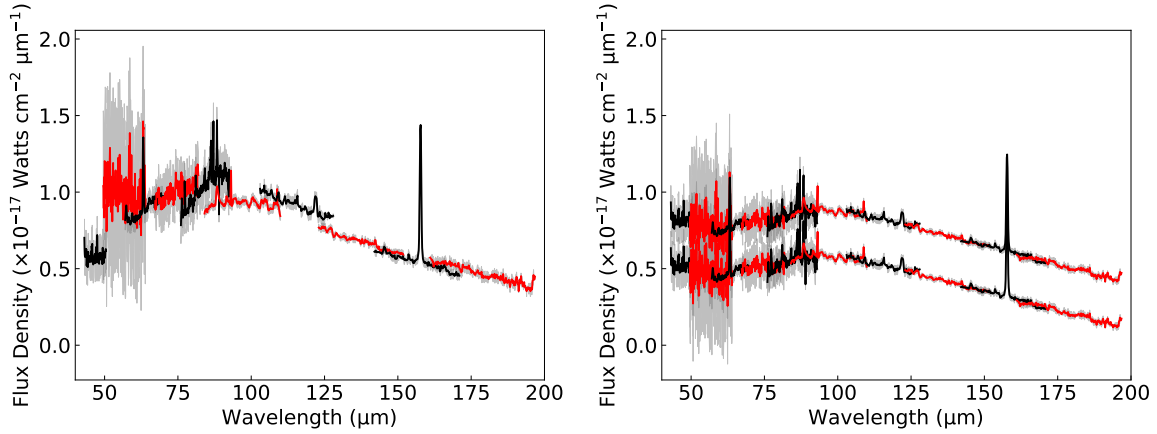


Figure 1. Left Panel: The *ISO* LWS spectrum of RCW 103 taken directly from the *ISO* Data Archive. The alternating red and black colors represent different subdetector spectra. Right Panel: The same spectrum as the left panel with the extended source correction and subdetector matching applied. Applying relative normalizations among the individual subdetector spectra results in a range of flux levels of the overall spectrum. The upper and lower bound flux levels are shown. The extended source corrections reduce the overall flux level by $\sim 30\%$ on average.

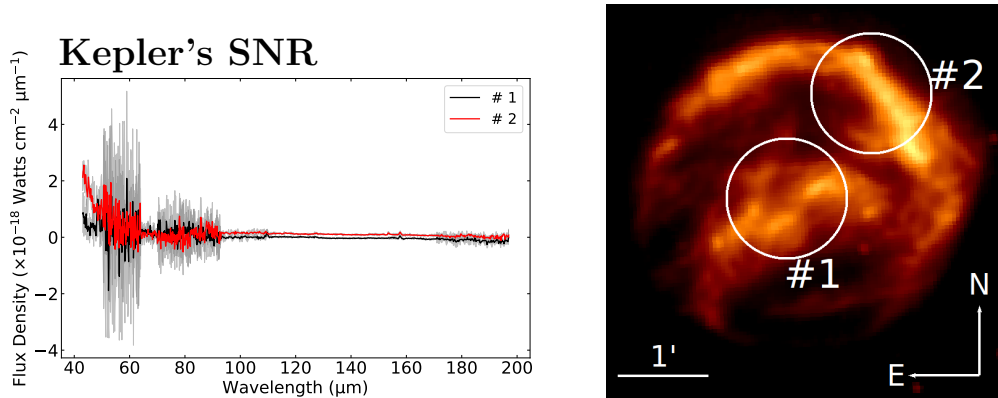


Figure 2. Left: The *ISO* LWS spectra of Kepler's SNR. Right: The *Spitzer* MIPS 24 μm image of Kepler's SNR. Two *ISO* LWS pointings are shown with white circles.

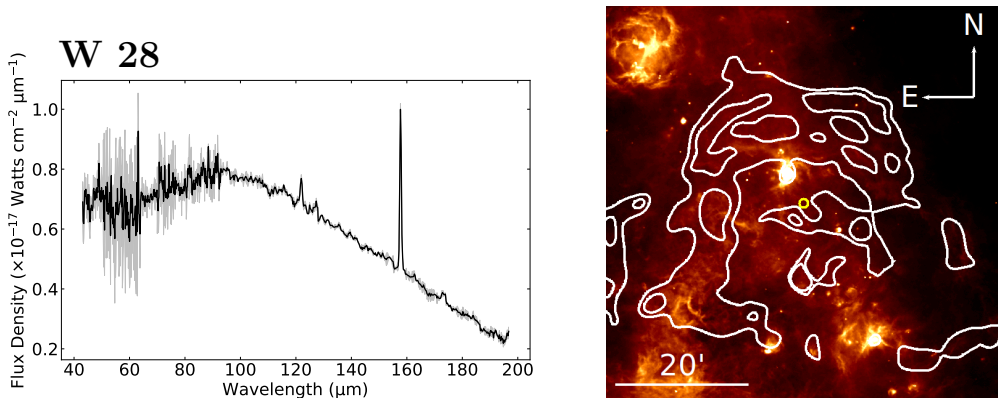


Figure 3. Left: The *ISO* LWS spectrum of W 28. Right: The *Herschel* PACS 70 μm image of W 28. The *ISO* LWS pointing is shown with a yellow circle. The white contours are from a VLA 325 MHz image.

¹<https://www.cosmos.esa.int/web/iso/highly-processed-data-products>

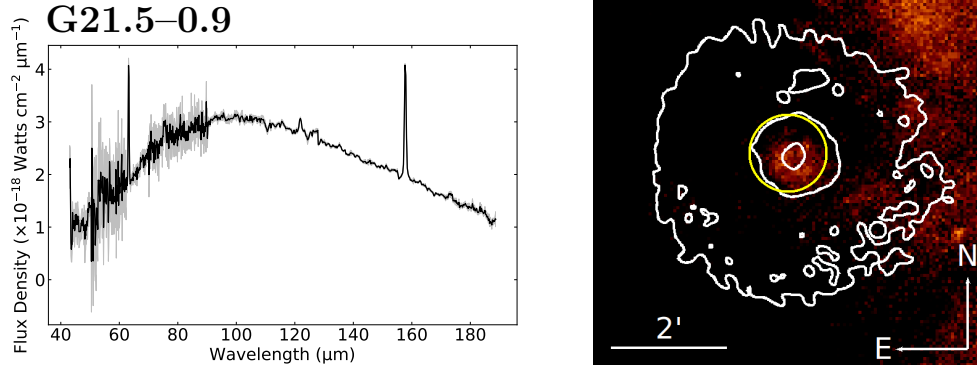


Figure 4. Left: The *ISO* LWS spectrum of G21.5-0.9. Right: The *Herschel* PACS 70 μm image of G21.5-0.9. The *ISO* LWS pointing is shown with a yellow circle. The white contours are from a *Chandra* (0.5 – 7.0 keV) image.

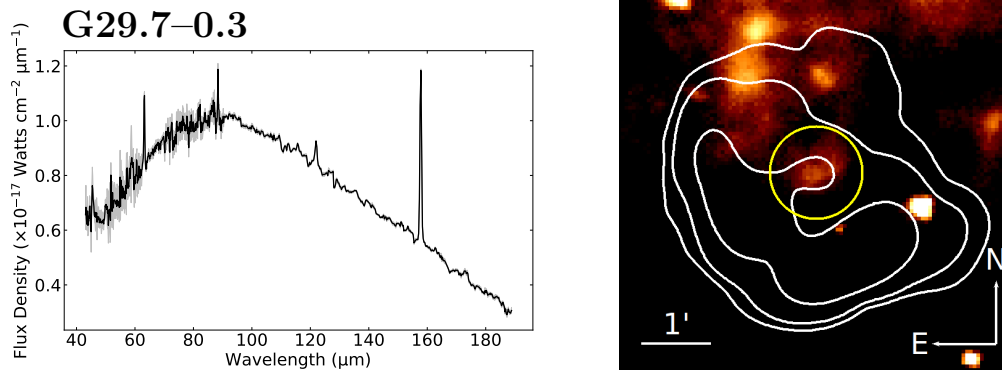


Figure 5. Left: The *ISO* LWS spectrum of G29.7-0.3. Right: The *Herschel* PACS 70 μm image of G29.7-0.3. The *ISO* LWS pointing is shown with a yellow circle. The white contours are from a VLA (1.4 GHz) image.

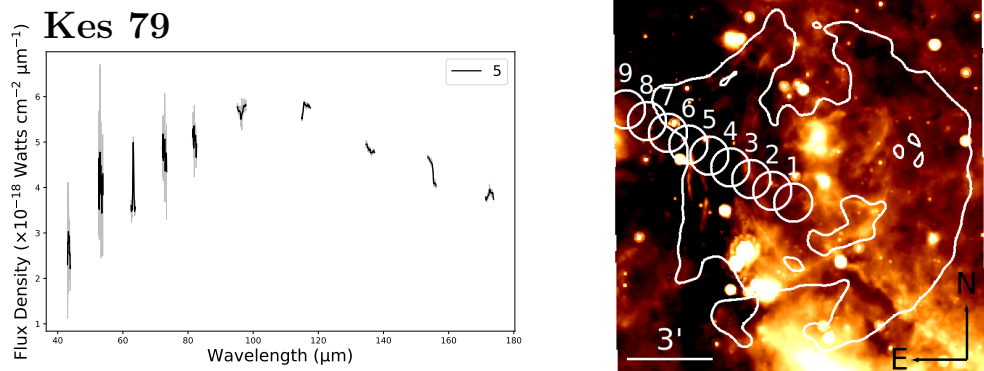


Figure 6. Left: The *ISO* LWS spectrum of Kes 79. Right: The *Spitzer* MIPS 24 μm image of Kes 79. The *ISO* LWS pointings are shown with white circles. The white contours are from a VLA (1.4 GHz) image. The raster spectra are shown in Figure 28.

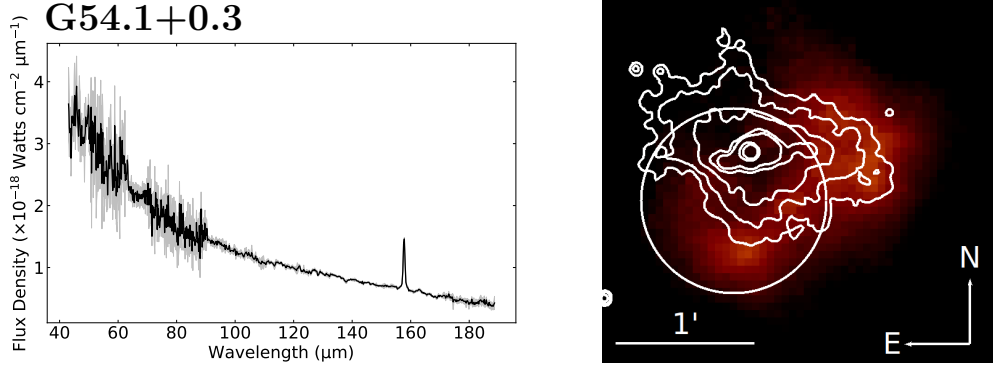


Figure 7. Left: The *ISO* LWS spectrum of G54.1+0.3. Right: The *Herschel* PACS 70 μm image of G54.1+0.3. The *ISO* LWS pointing is shown with a white circle. The white contours are from a *Chandra* (0.5 – 7.0 keV) image.

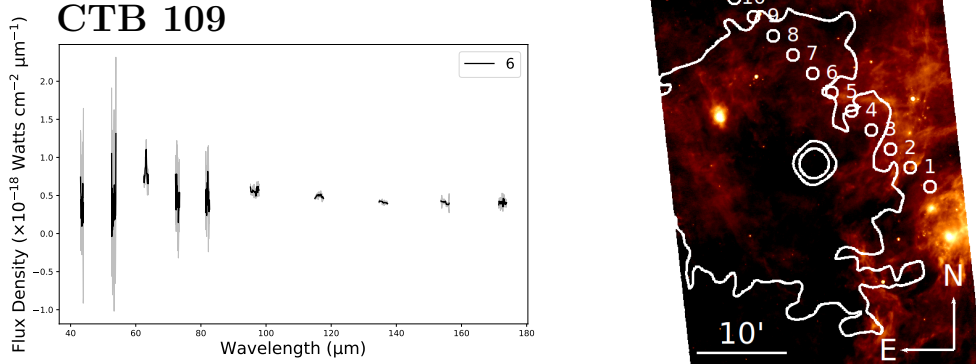


Figure 8. Left: The *ISO* LWS spectrum of CTB 109. Right: The *Spitzer* MIPS 24 μm image of CTB 109. The *ISO* LWS pointings are shown with white circles. The white contours are from an *XMM-Newton* (2.0 – 7.2 keV) image. The raster spectra are shown in Figure 28.

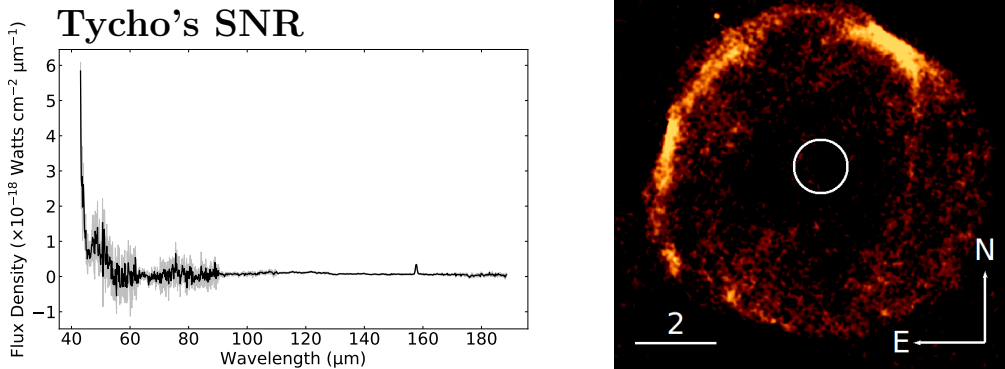


Figure 9. Left: The *ISO* LWS spectrum of Tycho's SNR. Right: The *Herschel* PACS 70 μm image of Tycho's SNR. The *ISO* LWS pointing is shown with a white circle.

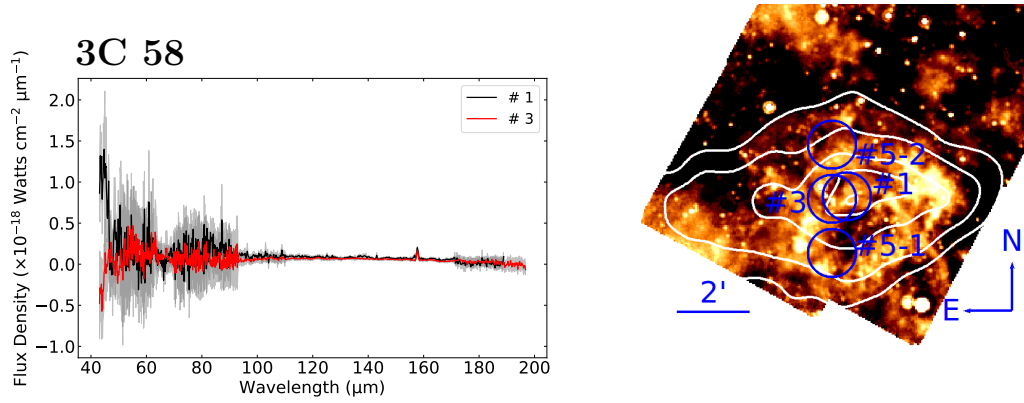


Figure 10. Left: The *ISO* LWS spectra of 3C 58. Right: The *Spitzer* MIPS 24 μm image of 3C 58. The *ISO* LWS pointings are shown with blue circles. The white contours are from a VLA (1.48 GHz) image.

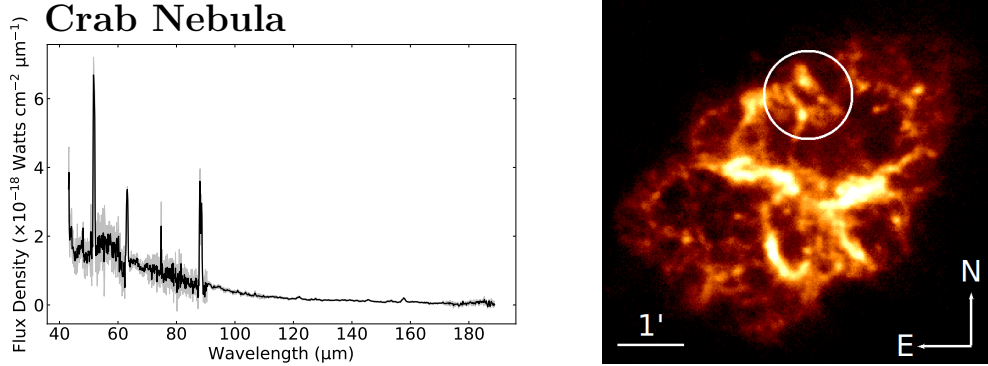


Figure 11. Left: The *ISO* LWS spectrum of Crab Nebula. Right: The *Herschel* PACS 70 μm image of the Crab Nebula. The *ISO* LWS pointing is shown with a white circle.

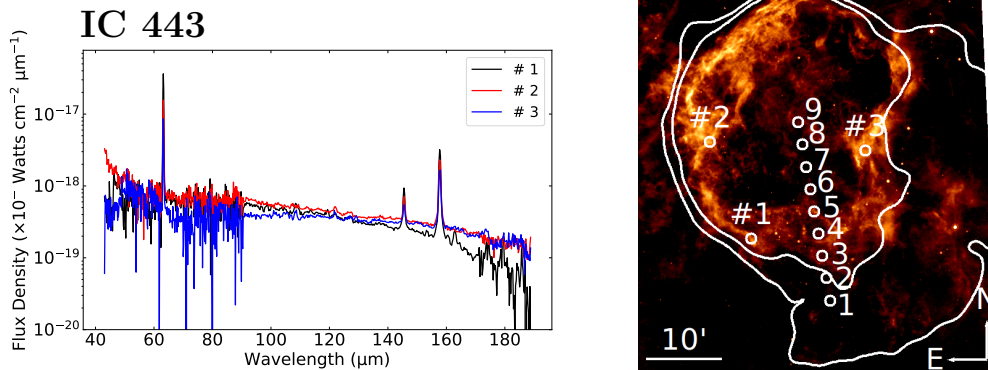


Figure 12. Left: The *ISO* LWS spectra of IC 443. Right: The *Spitzer* MIPS 24 μm image of IC 443. The *ISO* LWS pointings are shown with white circles. The raster line profiles are displayed in Figure 28. The white contours are from a VLA (330 MHz) image.

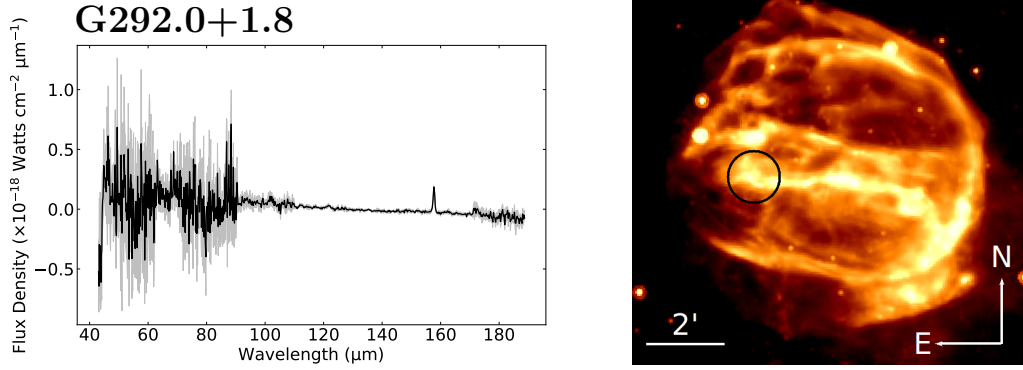


Figure 13. Left: The *ISO* LWS spectrum of G292.0+1.8. Right: The *Spitzer* MIPS 24 μm image of G292.0+1.8. The *ISO* LWS pointing is shown with a black circle.

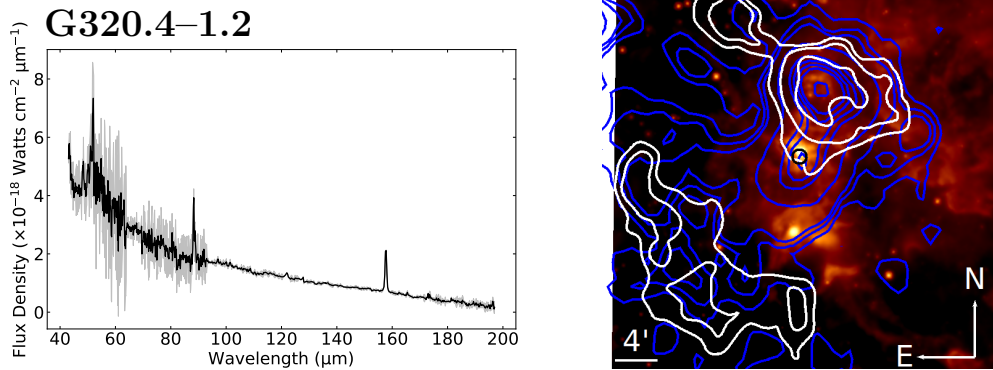


Figure 14. Left: The *ISO* LWS spectrum of G320.4-1.2. Right: The *WISE* 22 μm image of G320.4-1.2. The *ISO* LWS pointing is shown near the center with a black circle. The white contours are from a MOST (843 MHz) image. The blue contours are from a broadband *ROSAT* image.

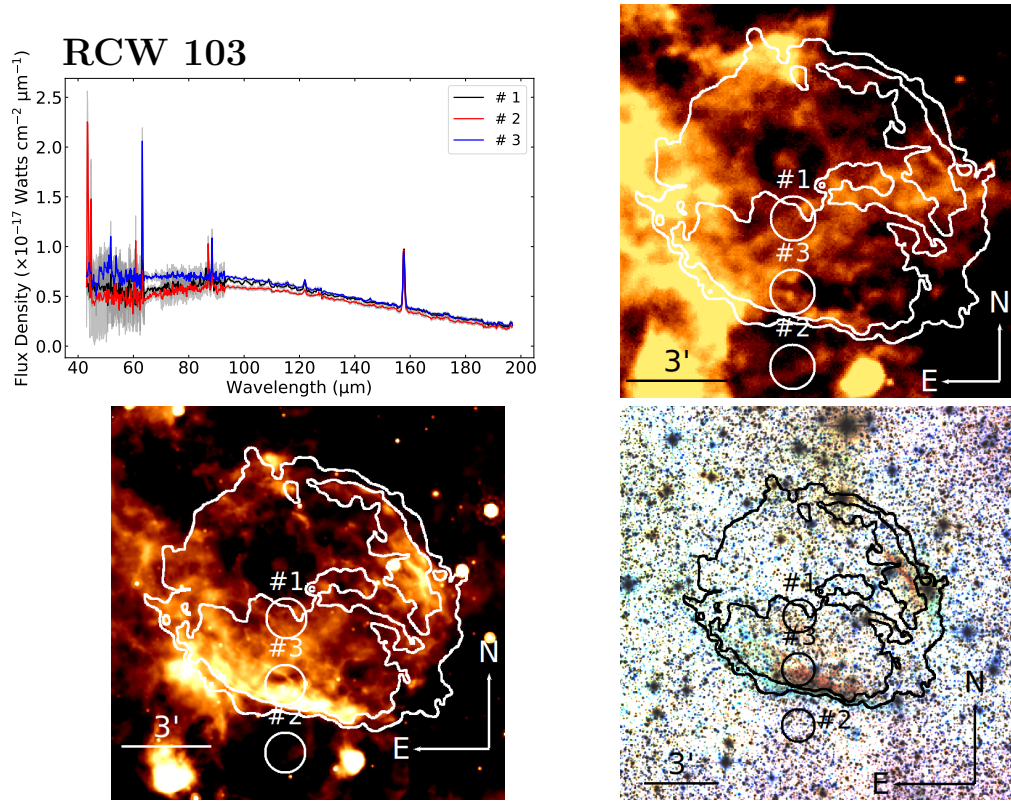


Figure 15. Upper Left: The *ISO* LWS spectra of RCW 103. Upper Right: The *Herschel* PACS 70 μm image of RCW 103. Lower Left: The *Spitzer* MIPS 24 μm image of RCW 103. Lower Right: The 3-color 2MASS image of RCW 103. The J, H, and K_s bands are shown in red, green, and blue, respectively. In all three image panels, the *ISO* LWS pointings are shown with white or black circles. The contours are from a *Chandra* (0.5 – 7.0 keV) image

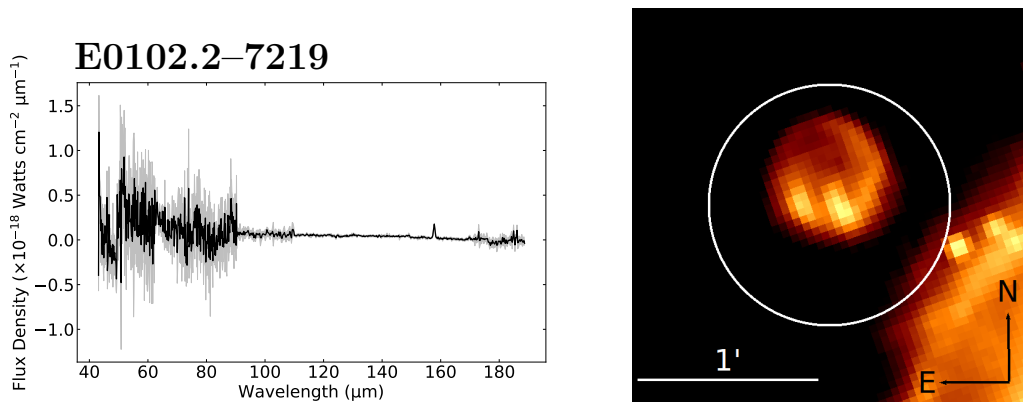


Figure 16. Left: The *ISO* LWS spectrum of E0102.2-7219. Right: The *Spitzer* MIPS 24 μm image of E0102.2-7219. The *ISO* LWS pointing is shown with a white circle.

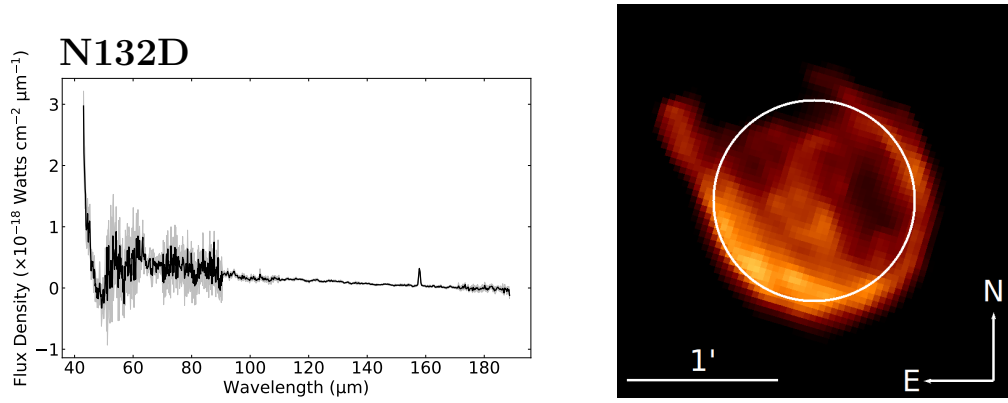


Figure 17. Left: The *ISO* LWS spectrum of N132D. Right: The *Spitzer* MIPS 24 μm image of N132D. The *ISO* LWS pointing is shown with a white circle.

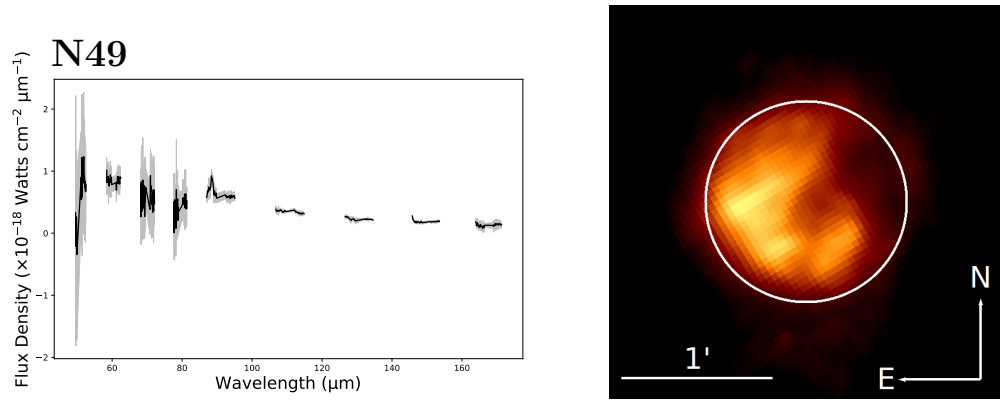


Figure 18. Left: The *ISO* LWS spectrum of N49. Right: The *Spitzer* MIPS 24 μm image of N49. The *ISO* LWS pointing is shown with a white circle.

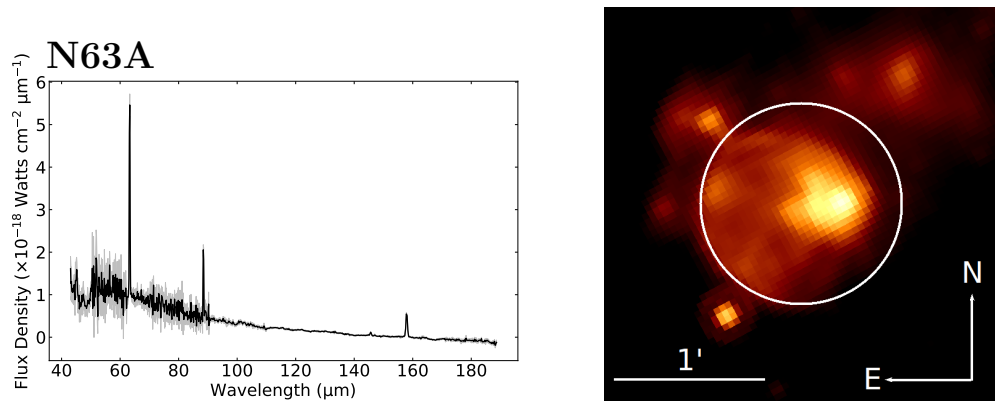


Figure 19. Left: The *ISO* LWS spectrum of N63A. Right: The *Spitzer* MIPS 24 μm image of N63A. The *ISO* LWS pointing is shown with a white circle.

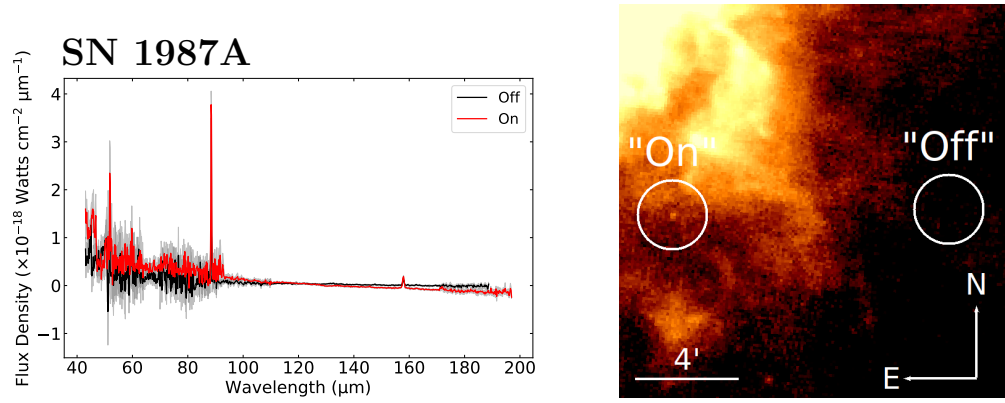


Figure 20. Left: The *ISO* LWS spectrum of SN 1987A. Right: The *Herschel* PACS 100 μm image of SN 1987A. The *ISO* LWS pointings are shown with white circles.

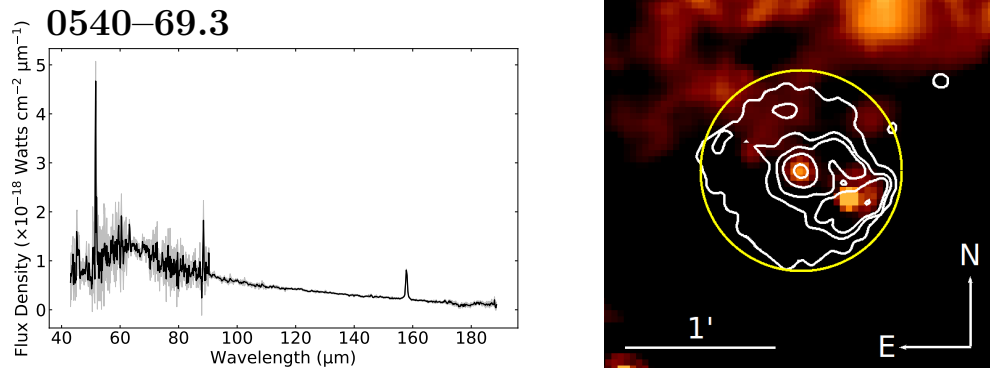


Figure 21. Left: The *ISO* LWS spectrum of 0540-69.3. Right: The *Spitzer* MIPS 24 μm image of 0540-69.3. The *ISO* LWS pointing is shown with a yellow circle. The white contours are from a Chandra (0.5 – 7.0 keV) image.

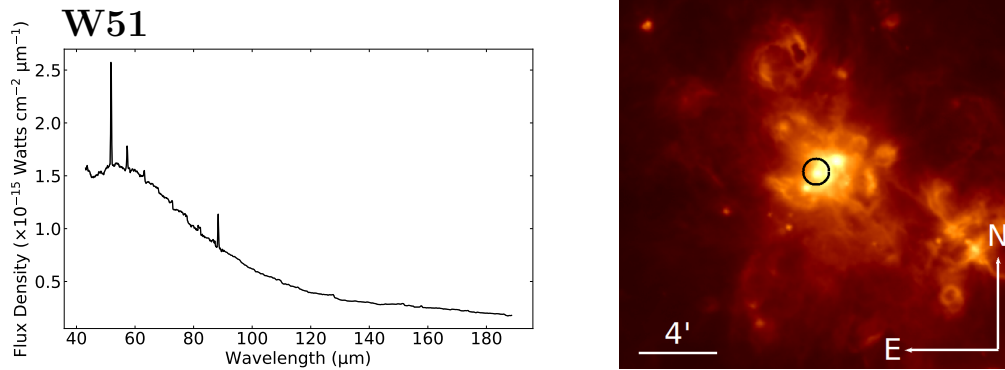


Figure 22. Left: The *ISO* LWS spectrum of W51. Right: The *Herschel* PACS 70 μm image of W51. The *ISO* LWS pointing is shown with a black circle.

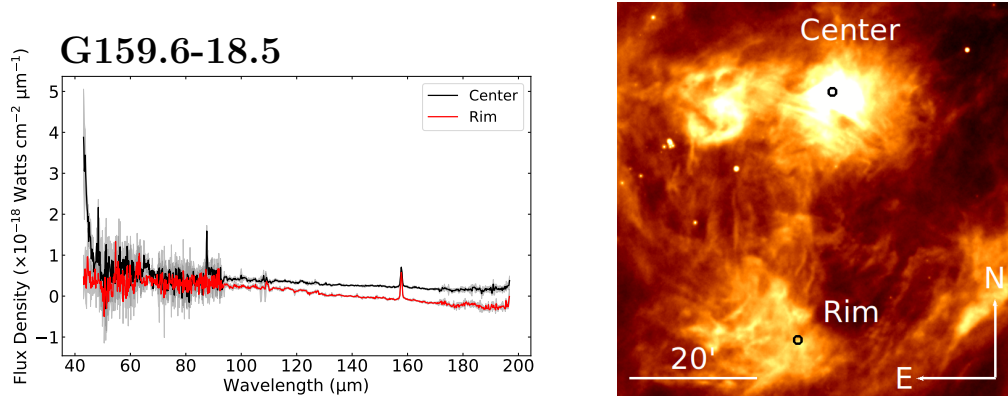


Figure 23. Left: The *ISO* LWS spectra of G159.6-18.5. Right: The *WISE* 22 μm image of G159.6-18.5. The *ISO* LWS pointings are shown with black circles.

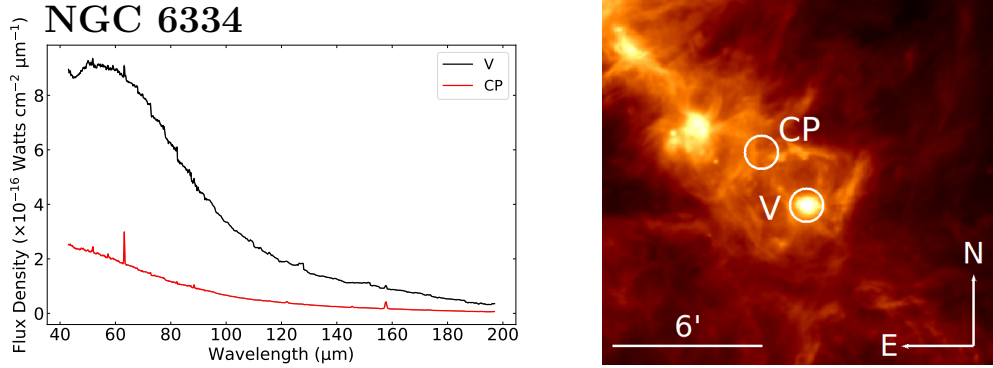


Figure 24. Left: The *ISO* LWS spectra of NGC 6334. Right: The *Herschel* PACS 70 μm image of NGC 6334. The *ISO* LWS pointings are shown with white circles.

Table 1. *ISO* LWS Observations of Our Sample of SNRs and HII Regions

Name	Target Name*	RA, DEC (J2000)	Date	t_{on} (s)	Publications	Figure
SNRs						
G4.5+6.8	Kepler # 1	17 ^h 30 ^m 41 ^s .79 -21°29'29".4	1996-02-16	814	This Work	2
G4.5+6.8	Kepler # 2	17 ^h 30 ^m 37 ^s .77 -21°28'19".7	1996-02-16	812	This Work	2
G6.4-0.1	W 28	18 ^h 00 ^m 38 ^s .65 -23°25'03".8	1996-02-24	814	This Work	3
G21.5-0.9	G21.5-0.9	18 ^h 33 ^m 34 ^s .08 -10°34'04".7	1996-10-11	1064	This Work	4
G29.7-0.3	G29.7-0.2	18 ^h 46 ^m 25 ^s .19 -02°58'33".9	1997-10-31	1126	3, This Work	5
G33.6+0.1	Kes 79 (L02)	18 ^h 52 ^m 54 ^s .00 +00°41'23".9	1996-10-04	1424	This Work	6
G54.1+0.3	G54.1+0.3	19 ^h 30 ^m 30 ^s .69 +18°51'53".1	1996-04-24	1052	This Work	7
G109.1-01.0	CTB 109 (L02)	23 ^h 02 ^m 17 ^s .27 +59°11'01".43	1997-02-23	1770	This Work	8
G120.1+1.4	Tycho #1	00 ^h 25 ^m 18 ^s .97 +64°08'22".06	1997-02-15	1114	This Work	9
G130.7+3.1	3C 58 #1	02 ^h 05 ^m 34 ^s .38 +64°49'49".7	1997-07-24	1126	This Work	10
G130.7+3.1	3C 58 #3	02 ^h 05 ^m 38 ^s .21 +64°49'45".1	1998-03-13	4036	This Work	10
G130.7+3.1	3C 58 #5	02 ^h 05 ^m 38 ^s .15 +64°48'14".98	1998-03-13	1332	This Work	10
G130.7+3.1	3C 58 Off (L02)	02 ^h 07 ^m 20 ^s .20 +64°38'44".99	1998-03-13	608	This Work	10

Table 1 continued

Table 1 (*continued*)

Name	Target Name*	RA, DEC (J2000)	Date	t_{on} (s)	Publications	Figure
G184.6-05.8	Crab Nebula	05 ^h 34 ^m 32 ^s .02 +22°02′04″.6	1998-02-19	1126	This Work	11
G189.1+3.0	IC 443 # 1	06 ^h 17 ^m 43 ^s .76 +22°21′59″.1	1998-02-26	1126	1, 2, This Work	12
G189.1+3.0	IC 443 # 2	06 ^h 18 ^m 7 ^s .45 +22°34′47″.42s	1998-02-27	1126	2, This Work	12
G189.1+3.0	IC 443 # 3	06 ^h 16 ^m 38 ^s .43 +22°33′36″.90	1998-02-27	1126	2, This Work	12
G189.1+3.0	IC443 - R10E STR (L02)	06 ^h 17 ^m 07 ^s .59 +22°25′34″.2	1998-03-18	2710	This Work	12
G292.0+1.8	G292.0+1.8	11 ^h 24 ^m 47 ^s .11 -59°15′44″.6	1996-09-02	1064	This Work	13
G320.4-1.2	G320.3-1.2	15 ^h 13 ^m 56 ^s .52 -59°08′10″.5	1996-02-20	812	This Work	14
G332.4-0.4	RCW 103 #1	16 ^h 17 ^m 41 ^s .84 -51°03′19″.8	1996-02-14	812	This Work	15
G332.4-0.4	RCW 103 #2 (Off)	16 ^h 17 ^m 42 ^s .04 -51°07′49″.7	1996-02-14	814	This Work	15
G332.4-0.4	RCW 103 #3	16 ^h 17 ^m 41 ^s .94 -51°05′34″.7	1996-02-20	812	This Work	15
J0104.1-7201	SMC-E0102.2-7219	01 ^h 04 ^m 02 ^s .16 -72°02′00″.5	1996-04-22	1052	This Work	16
J0525.0-6938	LMC-N132D	05 ^h 25 ^m 02 ^s .50 -69°38′38″.5	1996-05-06	1054	This Work	17
J0526.0-6604	LMC-N49 (L02)	05 ^h 26 ^m 00 ^s .57 -66°05′01″.7	1997-06-16	950	This Work	18
J0535.7-6602	LMC-N63A	05 ^h 35 ^m 43 ^s .15 -66°02′05″.8	1996-04-29	1054	This Work	19
J0535-6916	SN 1987A (Off)	05 ^h 34 ^m 28 ^s .13 -69°16′07″.3	1996-05-06	1052	This Work	20
J0535-6916	SN 1987A	05 ^h 35 ^m 28 ^s .04 -69°16′11″.6	1996-05-25	1552	2, This Work	20
J0535-6916	SN 1987A (L02)	05 ^h 35 ^m 28 ^s .04 -69°16′11″.7	1996-07-10	808	This Work	20
J0540.2-6920	LMC 0540-69.3	05 ^h 40 ^m 11 ^s .13 -69°19′54″.2	1996-05-06	1052	This Work	21
HII Regions						
G49.2-0.7	W51 FIR2	19 ^h 23 ^m 44 ^s .10 +14°30′33″.5	1997-04-24	2708	2, This Work	22
G159.6-18.5	G159 Center	03 ^h 39 ^m 57 ^s .95 +31°56′35″.5	1997-09-05	1180	This Work	23
G159.6-18.5	G159 Rim	03 ^h 40 ^m 23 ^s .35 +31°17′48″.1	1997-09-05	1180	This Work	23
G351.13-0.46	NGC6334 CP	17 ^h 20 ^m 06 ^s .31 -35°55′45″.80	1996-03-20	1110	This Work	24
G351.13-0.46	NGC6334 V	17 ^h 19 ^m 57 ^s .36 -35°57′52″.49	1996-03-20	1108	This Work	24
Planetary Nebulae						
G63.2+13.9	NGC6720	18 ^h 53 ^m 35 ^s .68 +33°01′40″.3	1996-11-16	1268	4, This Work	

NOTE— 1. (Snell et al. 2005) 2. (Liseau et al. 2006) 3. (He et al. 2005) 4. (Liu et al. 2001)

*The majority of targets were observed in the L01 mode, which covered the full range of the LWS detector. A few targets were observed in the L02 mode, which covered only certain wavelength bands specified by the observer.

Table 2. Observed Spectral Lines from *ISO* LWS Spectra of Supernova Remnants

Target	Wavelength (μm)	Line	FWHM (%) ^c (μm)	Surface Brightness (10^{-4} ergs $\text{s}^{-1}\text{cm}^{-2}\text{sr}^{-1}$)	Velocity ^a (km s^{-1})	Shift ^{b,k} (km s^{-1})
Kepler (#1)	157.73 ^{+0.01} _{-0.01}	[C II]	0.55 ^{+0.04} _{-0.03}	0.06 ^{+0.02} _{-0.01}
Kepler (#2) (<i>G4.5+6.8</i>)	^h 157.74 ^{+0.02} _{-0.02}	[C II]	0.56 ^{+0.09} _{-0.06}	0.08 ^{+0.02} _{-0.02}
W 28	^e 63.15 ^{+0.01} _{-0.01}	[O I]	0.31 ^{+0.02} _{-0.02} (12 ⁺⁷ ₋₇ %)	1.3 ^{+0.2} _{-0.1}	700 ⁺²⁰⁰ ₋₂₀₀	-160 ⁺⁶⁰ ₋₅₀
(<i>G6.4-0.1</i>)	121.92 ^{+0.02} _{-0.02}	[N II]	0.76 ^{+0.06} _{-0.05} (29 ⁺⁹ ₋₈ %)	0.8 ^{+0.2} _{-0.2}	1200 ⁺²⁰⁰ ₋₂₀₀	...
	^{e,i,g} 145.49 ^{+0.07} _{-0.04}	[O I]	0.60 ^{+0.09} _{-0.15}	0.14 ^{+0.09} _{-0.05}

Table 2 continued

Table 2 (continued)

Target	Wavelength (μm)	Line	FWHM (%) ^c (μm)	Surface Brightness (10^{-4} ergs s $^{-1}$ cm $^{-2}$ sr $^{-1}$)	Velocity ^a (km s $^{-1}$)	Shift ^{b,k} (km s $^{-1}$)	
G21.5-0.9	^g 157.73 $^{+0.02}_{-0.02}$	[C II]	0.74 $^{+0.03}_{-0.03}$ (27 $^{+5}_{-5}$ %)	4.7 $^{+0.7}_{-0.4}$	870 $^{+90}_{-90}$...	
	63.21 $^{+0.01}_{-0.01}$	[O I]	0.33 $^{+0.01}_{-0.01}$ (20 $^{+3}_{-3}$ %)	1.06 $^{+0.08}_{-0.08}$	900 $^{+90}_{-80}$	130 $^{+20}_{-20}$	
	^g 121.83 $^{+0.03}_{-0.04}$	[N II]	0.94 $^{+0.11}_{-0.09}$ (61 $^{+18}_{-15}$ %)	0.32 $^{+0.06}_{-0.04}$	1800 $^{+400}_{-300}$	-180 $^{+80}_{-100}$	
G29.7-0.3 (Kes 75)	^f 145.59 $^{+0.04}_{-0.04}$	[O I]	0.74 $^{+0.10}_{-0.09}$ (25 $^{+16}_{-16}$ %)	0.10 $^{+0.02}_{-0.02}$	900 $^{+300}_{-300}$	130 $^{+80}_{-90}$	
	^g 157.76 $^{+0.01}_{-0.01}$	[C II]	0.66 $^{+0.01}_{-0.01}$ (13 $^{+2}_{-2}$ %)	1.35 $^{+0.05}_{-0.05}$	600 $^{+50}_{-50}$	40 $^{+9}_{-9}$	
	63.20 $^{+0.01}_{-0.01}$	[O I]	0.29 $^{+0.02}_{-0.02}$	1.08 $^{+0.16}_{-0.09}$	
	88.39 $^{+0.01}_{-0.01}$	[O III]	0.29 $^{+0.03}_{-0.03}$	0.7 $^{+0.2}_{-0.2}$...	140 $^{+40}_{-50}$	
	121.96 $^{+0.01}_{-0.01}$	[N II]	0.77 $^{+0.04}_{-0.04}$ (32 $^{+6}_{-6}$ %)	0.85 $^{+0.07}_{-0.07}$	1200 $^{+140}_{-130}$	160 $^{+30}_{-30}$	
G54.1+0.3	^f 145.59 $^{+0.05}_{-0.04}$	[O I]	0.85 $^{+0.11}_{-0.09}$ (46 $^{+18}_{-15}$ %)	0.28 $^{+0.07}_{-0.04}$	1300 $^{+300}_{-300}$	100 $^{+90}_{-80}$	
	^g 157.78 $^{+0.01}_{-0.01}$	[C II]	0.631 $^{+0.009}_{-0.009}$ (8 $^{+1}_{-1}$ %)	5.24 $^{+0.13}_{-0.13}$	460 $^{+40}_{-40}$	60 $^{+10}_{-10}$	
	63.18 $^{+0.01}_{-0.01}$	[O I]	0.297 $^{+0.03}_{-0.03}$	0.19 $^{+0.04}_{-0.02}$	
	^{d,e} 88.39 $^{+0.04}_{-0.09}$	[O III]	0.56 $^{+0.17}_{-0.09}$	0.13 $^{+0.05}_{-0.04}$	
	122.03 $^{+0.03}_{-0.02}$	[N II]	0.44 $^{+0.04}_{-0.04}$	0.04 $^{+0.01}_{-0.01}$...	330 $^{+60}_{-60}$	
Tycho # 1 (G120.1+1.4)	157.74 $^{+0.01}_{-0.01}$	[C II]	0.67 $^{+0.01}_{-0.01}$ (15 $^{+1}_{-1}$ %)	0.72 $^{+0.03}_{-0.03}$	640 $^{+40}_{-40}$...	
	157.72 $^{+0.01}_{-0.01}$	[C II]	0.62 $^{+0.01}_{-0.01}$ (5 $^{+2}_{-2}$ %)	0.24 $^{+0.01}_{-0.01}$	370 $^{+80}_{-80}$...	
3C 58 (#1) (G130.7+3.1)	^e 157.75 $^{+0.03}_{-0.03}$	[C II]	0.60 $^{+0.06}_{-0.05}$	0.10 $^{+0.02}_{-0.02}$	
3C 58 (#3)	157.72 $^{+0.01}_{-0.01}$	[C II]	0.58 $^{+0.02}_{-0.02}$	0.09 $^{+0.01}_{-0.01}$	
^j 3C 58 (#5 Raster 1)	157.74 $^{+0.02}_{-0.02}$	[C II]	0.67 $^{+0.04}_{-0.04}$ (14 $^{+7}_{-7}$ %)	0.07 $^{+0.01}_{-0.01}$	600 $^{+200}_{-100}$...	
^j 3C 58 (#5 Raster 2)	157.74 $^{+0.01}_{-0.01}$	[C II]	0.59 $^{+0.03}_{-0.03}$	0.07 $^{+0.01}_{-0.01}$	
Crab Nebula (G184.6-05.8)	51.79 $^{+0.01}_{-0.01}$	[O III]	0.55 $^{+0.03}_{-0.03}$ (109 $^{+12}_{-12}$ %)	3.7 $^{+0.4}_{-0.3}$	2800 $^{+200}_{-200}$	-160 $^{+70}_{-70}$	
	^l (blue-shifted)	51.66 $^{+0.02}_{-0.02}$	[O III]	0.32 $^{+0.05}_{-0.04}$ (22 $^{+19}_{-15}$ %)	2.1 $^{+0.4}_{-0.4}$	1100 $^{+500}_{-400}$	-900 $^{+100}_{-100}$
^l (red-shifted)	51.98 $^{+0.02}_{-0.02}$	[O III]	0.26 $^{+0.04}_{-0.03}$	1.3 $^{+0.4}_{-0.4}$...	900 $^{+100}_{-100}$	
^l (blue-shifted)	63.13 $^{+0.01}_{-0.01}$	[O I]	0.56 $^{+0.02}_{-0.02}$ (102 $^{+7}_{-7}$ %)	1.51 $^{+0.09}_{-0.09}$	2300 $^{+100}_{-100}$	-300 $^{+50}_{-50}$	
	88.23 $^{+0.02}_{-0.02}$	[O III]	1.01 $^{+0.07}_{-0.06}$ (255 $^{+23}_{-22}$ %)	4.1 $^{+0.5}_{-0.5}$	3300 $^{+200}_{-200}$	-430 $^{+70}_{-70}$	
	88.02 $^{+0.01}_{-0.01}$	[O III]	0.39 $^{+0.03}_{-0.03}$ (38 $^{+11}_{-11}$ %)	1.6 $^{+0.2}_{-0.1}$	900 $^{+200}_{-100}$	-1120 $^{+40}_{-50}$	
	^l (red-shifted)	88.57 $^{+0.01}_{-0.01}$	[O III]	0.41 $^{+0.04}_{-0.03}$ (45 $^{+14}_{-11}$ %)	1.4 $^{+0.2}_{-0.1}$	1000 $^{+200}_{-200}$	730 $^{+30}_{-40}$
	^e 121.91 $^{+0.05}_{-0.05}$	[N II]	1.0 $^{+0.2}_{-0.2}$ (73 $^{+32}_{-29}$ %)	0.10 $^{+0.03}_{-0.03}$	2000 $^{+600}_{-500}$...	
IC 443 (#1) (G189.1+3.0)	145.5 $^{+0.1}_{-0.1}$	[O I]	1.5 $^{+0.5}_{-0.3}$ (160 $^{+80}_{-49}$ %)	0.09 $^{+0.04}_{-0.02}$	2900 $^{+1100}_{-600}$...	
	157.69 $^{+0.03}_{-0.03}$	[C II]	1.09 $^{+0.07}_{-0.07}$ (87 $^{+12}_{-11}$ %)	0.15 $^{+0.02}_{-0.02}$	1800 $^{+200}_{-100}$	-90 $^{+60}_{-60}$	
	63.19 $^{+0.01}_{-0.01}$	[O I]	0.280 $^{+0.002}_{-0.002}$	13.2 $^{+0.3}_{-0.3}$	
IC 443 (#2) (G189.1+3.0)	^f 145.55 $^{+0.01}_{-0.01}$	[O I]	0.72 $^{+0.03}_{-0.03}$ (23 $^{+5}_{-5}$ %)	0.62 $^{+0.05}_{-0.05}$	900 $^{+100}_{-100}$	50 $^{+20}_{-20}$	
	^g 157.73 $^{+0.01}_{-0.01}$	[C II]	0.67 $^{+0.02}_{-0.02}$ (14 $^{+2}_{-2}$ %)	2.56 $^{+0.1}_{-0.09}$	600 $^{+60}_{-60}$...	
IC 443 (#3) (G189.1+3.0)	^g 63.20 $^{+0.01}_{-0.01}$	[O I]	0.295 $^{+0.005}_{-0.005}$ (6 $^{+1}_{-1}$ %)	5.8 $^{+0.3}_{-0.3}$	500 $^{+70}_{-70}$	90 $^{+20}_{-20}$	
	^e 121.93 $^{+0.06}_{-0.07}$	[N II]	1.2 $^{+0.3}_{-0.3}$ (111 $^{+50}_{-43}$ %)	0.15 $^{+0.04}_{-0.04}$	2700 $^{+800}_{-700}$...	
	145.52 $^{+0.01}_{-0.01}$	[O I]	0.66 $^{+0.02}_{-0.01}$ (13 $^{+2}_{-2}$ %)	0.33 $^{+0.02}_{-0.02}$	640 $^{+60}_{-60}$...	
IC 443 (#3) (G189.1+3.0)	^g 157.75 $^{+0.01}_{-0.01}$	[C II]	0.67 $^{+0.02}_{-0.02}$ (15 $^{+4}_{-4}$ %)	1.8 $^{+0.2}_{-0.2}$	640 $^{+100}_{-90}$...	
	63.18 $^{+0.01}_{-0.01}$	[O I]	0.274 $^{+0.006}_{-0.005}$	2.89 $^{+0.09}_{-0.07}$	
	^e 122.02 $^{+0.07}_{-0.06}$	[N II]	1.1 $^{+0.3}_{-0.2}$ (94 $^{+57}_{-36}$ %)	0.09 $^{+0.03}_{-0.02}$	2400 $^{+1000}_{-600}$	300 $^{+200}_{-200}$	
IC 443 (#3) (G189.1+3.0)	145.52 $^{+0.02}_{-0.02}$	[O I]	0.77 $^{+0.04}_{-0.04}$ (31 $^{+6}_{-6}$ %)	0.25 $^{+0.03}_{-0.03}$	1000 $^{+100}_{-100}$...	
	157.75 $^{+0.01}_{-0.01}$	[C II]	0.68 $^{+0.01}_{-0.01}$ (16 $^{+2}_{-1}$ %)	0.88 $^{+0.04}_{-0.04}$	670 $^{+40}_{-40}$...	

Table 2 continued

Table 2 (continued)

Target	Wavelength (μm)	Line	FWHM (%) ^c (μm)	Surface Brightness (10^{-4} ergs s ⁻¹ cm ⁻² sr ⁻¹)	Velocity ^a (km s ⁻¹)	Shift ^{b,k} (km s ⁻¹)
G292.0+1.8	^e 63.22 ^{+0.02} _{-0.03}	[O I]	0.29 ^{+0.07} _{-0.06}	0.14 ^{+0.07} _{-0.04}
	88.37 ^{+0.03} _{-0.02}	[O III]	0.17 ^{+0.05} _{-0.06}	0.21 ^{+0.11} _{-0.08}
	^g 157.73 ^{+0.01} _{-0.01}	[C II]	0.61 ^{+0.02} _{-0.02}	0.16 ^{+0.01} _{-0.01}
G320.4-1.2	^{e,g,i} 63.15 ^{+0.03} _{-0.04}	[O I]	0.29 ^{+0.08} _{-0.06}	0.3 ^{+0.1} _{-0.1}
	88.28 ^{+0.03} _{-0.03}	[O III]	0.66 ^{+0.06} _{-0.06} (137 ⁺²⁰ ₋₂₀ %)	1.2 ^{+0.1} _{-0.1}	2100 ⁺²⁰⁰ ₋₂₀₀	-240 ⁺⁹⁰ ₋₉₀
	121.95 ^{+0.02} _{-0.03}	[N II]	0.9 ^{+0.1} _{-0.1} (62 ⁺²² ₋₁₉ %)	0.18 ^{+0.03} _{-0.03}	1800 ⁺⁴⁰⁰ ₋₄₀₀	120 ⁺⁶⁰ ₋₇₀
	^g 157.70 ^{+0.01} _{-0.01}	[C II]	0.629 ^{+0.006} _{-0.006} (7 ⁺¹ ₋₁ %)	1.21 ^{+0.02} _{-0.02}	400 ⁺³⁰ ₋₃₀	-78 ⁺⁹ ₋₉
RCW 103 (# 1) (G332.4-0.4)	63.20 ^{+0.01} _{-0.01}	[O I]	0.32 ^{+0.01} _{-0.01} (17 ⁺³ ₋₃ %)	1.53 ^{+0.11} _{-0.07}	800 ⁺⁹⁰ ₋₉₀	100 ⁺³⁰ ₋₃₀
	88.30 ^{+0.02} _{-0.02}	[O III]	0.23 ^{+0.05} _{-0.04}	0.7 ^{+0.3} _{-0.2}	...	-180 ⁺⁶⁰ ₋₆₀
	121.87 ^{+0.02} _{-0.02}	[N II]	0.89 ^{+0.04} _{-0.04} (51 ⁺⁶ ₋₆ %)	0.9 ^{+0.1} _{-0.1}	1600 ⁺¹⁰⁰ ₋₁₀₀	...
	ⁱ 145.49 ^{+0.04} _{-0.04}	[O I]	0.64 ^{+0.06} _{-0.06}	0.23 ^{+0.05} _{-0.05}
	^g 157.73 ^{+0.01} _{-0.01}	[C II]	0.70 ^{+0.01} _{-0.01} (20 ⁺¹ ₋₁ %)	5.7 ^{+0.2} _{-0.2}	750 ⁺⁴⁰ ₋₄₀	...
RCW 103 (# 3) (G332.4-0.4)	51.84 ^{+0.04} _{-0.03}	[O III]	0.27 ^{+0.08} _{-0.06}	1.2 ^{+1.0} _{-1.0}
	63.17 ^{+0.01} _{-0.01}	[O I]	0.28 ^{+0.01} _{-0.01}	5.3 ^{+0.7} _{-0.7}	...	-80 ⁺³⁰ ₋₃₀
	88.42 ^{+0.01} _{-0.01}	[O III]	0.30 ^{+0.02} _{-0.02}	1.6 ^{+0.5} _{-0.2}	...	200 ⁺³⁰ ₋₃₀
	^e 121.97 ^{+0.03} _{-0.03}	[N II]	0.98 ^{+0.11} _{-0.16} (68 ⁺¹⁹ ₋₂₈ %)	0.9 ^{+0.2} _{-0.2}	2000 ⁺³⁰⁰ ₋₅₀₀	180 ⁺⁷⁰ ₋₈₀
	ⁱ 145.44 ^{+0.03} _{-0.04}	[O I]	0.65 ^{+0.10} _{-0.09}	0.33 ^{+0.06} _{-0.05}	...	-180 ⁺⁷⁰ ₋₈₀
E0102.2-7219 (J0104.1-7201)	157.72 ^{+0.01} _{-0.01}	[C II]	0.74 ^{+0.02} _{-0.02} (26 ⁺³ ₋₃ %)	5.6 ^{+0.4} _{-0.4}	850 ⁺⁷⁰ ₋₆₀	-50 ⁺¹⁰ ₋₁₀
	^d 88.29 ^{+0.05} _{-0.04}	[O III]	0.7 ^{+0.1} _{-0.1} (20 ⁺²¹ ₋₁₈ %)	0.16 ^{+0.04} _{-0.04}	1300 ⁺⁸⁰⁰ ₋₆₀₀	-400 ⁺²⁰⁰ ₋₁₀₀
	157.78 ^{+0.01} _{-0.01}	[C II]	0.60 ^{+0.03} _{-0.03}	0.11 ^{+0.01} _{-0.01}	...	-90 ⁺²⁰ ₋₂₀
N132D (J0525.0-6938)	^e 63.27 ^{+0.02} _{-0.02}	[O I]	0.43 ^{+0.05} _{-0.04} (54 ⁺¹⁷ ₋₁₆ %)	0.18 ^{+0.05} _{-0.03}	1500 ⁺³⁰⁰ ₋₃₀₀	...
	157.87 ^{+0.01} _{-0.01}	[C II]	0.61 ^{+0.01} _{-0.01} (4 ⁺¹ ₋₁ %)	0.23 ^{+0.01} _{-0.01}	330 ⁺⁷⁰ ₋₇₀	...
^j N49 (J0526.0-6604)	^e 88.50 ^{+0.07} _{-0.09}	[O III]	1.1 ^{+0.6} _{-0.4} (90 ⁺¹⁰³ ₋₆₈ %)	0.4 ^{+0.2} _{-0.1}	3000 ⁺²⁰⁰⁰ ₋₁₀₀₀	...
N63A (J0535.7-6602)	63.26 ^{+0.01} _{-0.01}	[O I]	0.264 ^{+0.009} _{-0.009}	1.73 ^{+0.13} _{-0.08}	...	100 ⁺²⁰ ₋₂₀
	88.45 ^{+0.01} _{-0.01}	[O III]	0.276 ^{+0.018} _{-0.015}	0.63 ^{+0.09} _{-0.08}
	145.75 ^{+0.02} _{-0.03}	[O I]	0.60 ^{+0.06} _{-0.06}	0.076 ^{+0.012} _{-0.012}	...	180 ⁺⁵⁰ ₋₆₀
SN1987A (J0535-6916)	157.94 ^{+0.01} _{-0.01}	[C II]	0.563 ^{+0.01} _{-0.01}	0.42 ^{+0.02} _{-0.02}	...	90 ⁺¹⁰ ₋₁₀
	^e 51.86 ^{+0.02} _{-0.02}	[O III]	0.26 ^{+0.04} _{-0.04}	0.7 ^{+0.2} _{-0.2}
	88.48 ^{+0.01} _{-0.01}	[O III]	0.29 ^{+0.01} _{-0.01}	1.5 ^{+0.2} _{-0.2}	...	160 ⁺¹⁰ ₋₁₀
^j SN1987A (L02)	157.88 ^{+0.01} _{-0.01}	[C II]	0.62 ^{+0.02} _{-0.02}	0.20 ^{+0.01} _{-0.01}
	51.87 ^{+0.01} _{-0.01}	[O III]	0.30 ^{+0.03} _{-0.03}	0.7 ^{+0.1} _{-0.1}
0540-69.3 (J0535.7-6602)	157.87 ^{+0.01} _{-0.01}	[C II]	0.60 ^{+0.02} _{-0.02}	0.19 ^{+0.01} _{-0.01}
	^e 51.64 ^{+0.03} _{-0.03}	[O III]	0.59 ^{+0.12} _{-0.09} (91 ⁺³⁸ ₋₂₉ %)	1.8 ^{+0.6} _{-0.5}	2900 ⁺⁸⁰⁰ ₋₆₀₀	-1300 ⁺²⁰⁰ ₋₂₀₀
	63.22 ^{+0.01} _{-0.01}	[O I]	0.26 ^{+0.02} _{-0.02}	0.18 ^{+0.02} _{-0.02}	...	-90 ⁺⁶⁰ ₋₅₀
	^e 88.47 ^{+0.02} _{-0.02}	[O III]	0.32 ^{+0.05} _{-0.05}	0.4 ^{+0.2} _{-0.1}
	157.88 ^{+0.01} _{-0.01}	[C II]	0.64 ^{+0.03} _{-0.02} (6 ⁺² ₋₂ %)	0.47 ^{+0.03} _{-0.03}	400 ⁺¹⁰⁰ ₋₁₀₀	...

Table 2 continued

Table 2 (*continued*)

Target	Wavelength (μm)	Line	FWHM (%) ^c (μm)	Surface Brightness ($10^{-4} \text{ ergs s}^{-1} \text{ cm}^{-2} \text{ sr}^{-1}$)	Velocity ^a (km s^{-1})	Shift ^{b,k} (km s^{-1})
--------	---------------------------------	------	--	---	---	--

^aEstimated velocity dispersion after accounting for instrumental resolution.

^bDoppler shift from the line centroid.

^cPercent broader than instrument resolution.

^dValues are estimated from detector LW1.

^eLess than 5σ detection.

^fNo line-broadening detected in adjacent subdetector.

^gHigh reduced chi-squared value ($\gtrsim 2$).

^hLow reduced chi-squared value ($\lesssim 0.1$).

ⁱLine not detected in adjacent subdetector.

^jL02 mode observation.

^kFor remnants in the SMC or LMC, the Doppler-shift due to the motion of the galaxy has been subtracted.

^lThe best-fit results for two-Gaussian + linear component model fits to each of the [O III] 52 and 88 μm lines are shown.

... Value is approximately zero.

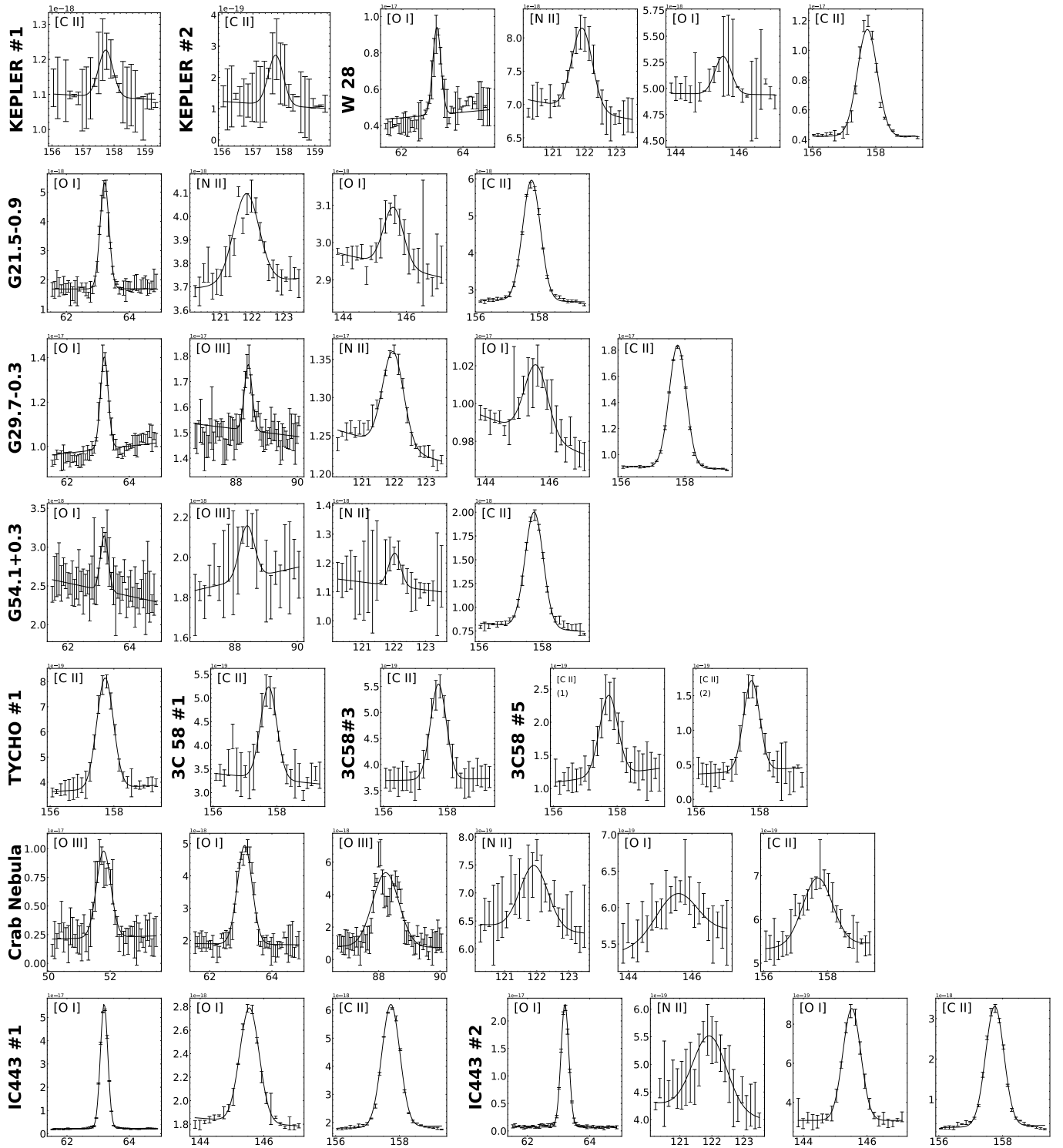


Figure 25. FIR Lines of SNRs. The best-fit Gaussian + linear model is overlaid. The y-axis is in units of flux density ($\text{erg s}^{-1} \text{cm}^{-2} \text{sr}^{-1}$) and x-axis in units of wavelength (μm).

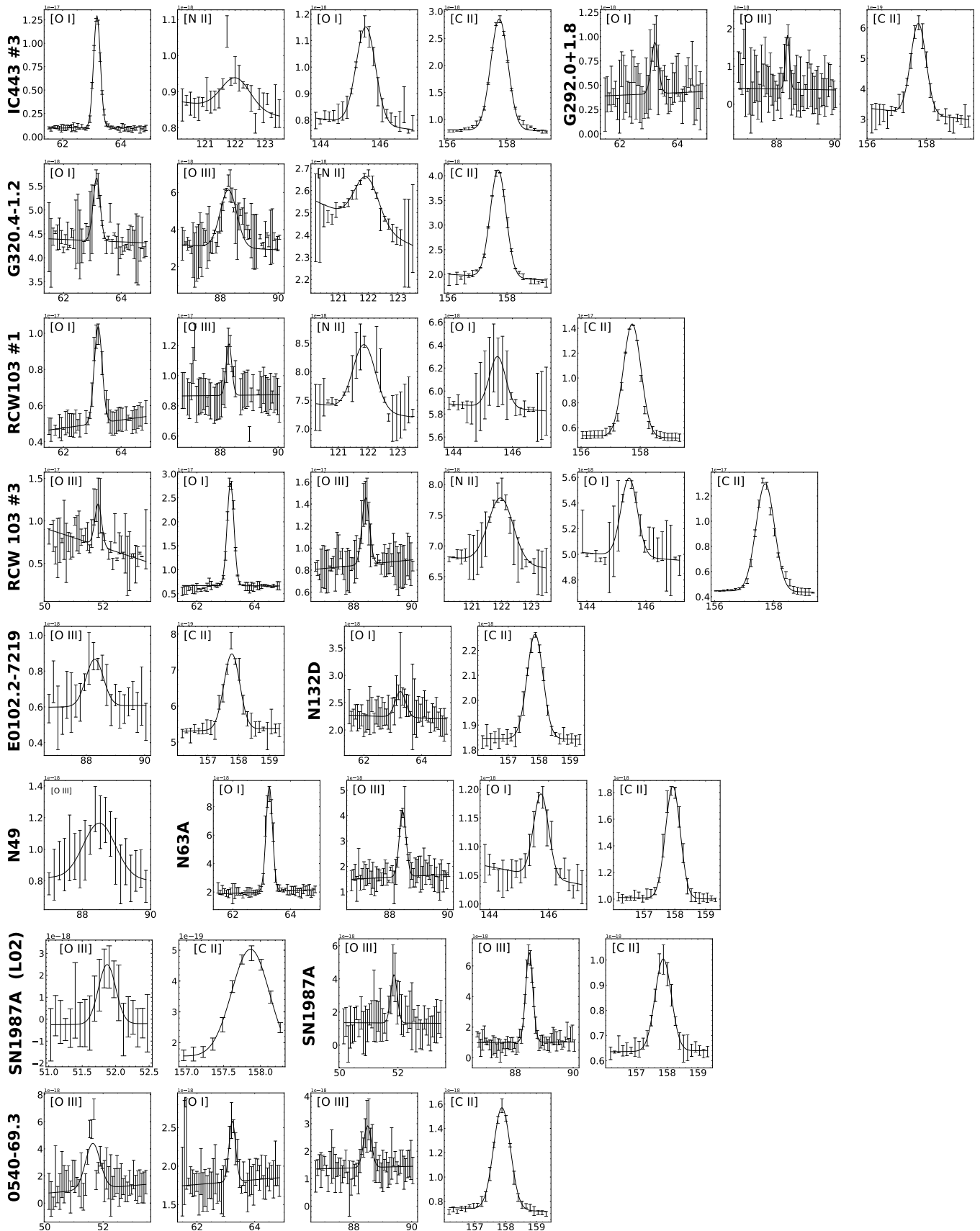


Figure 26. FIR Lines of SNRs (continued)

Table 3. Observed Spectral Lines from *ISO* LWS Spectra of HII Regions and PN NGC 6720

Target	Wavelength (μm)	Line	FWHM (%) ^c (μm)	Surface Brightness (10^{-4} ergs s ⁻¹ cm ⁻² sr ⁻¹)
W51	51.82 ^{+0.01} _{-0.01}	[O III]	0.283 ^{+0.004} _{-0.004}	289 ⁺⁸ ₋₈
	63.17 ^{+0.01} _{-0.01}	[O I]	0.283 ^{+0.009} _{-0.008}	41 ⁺² ₋₂
	88.39 ^{+0.01} _{-0.01}	[O III]	0.287 ^{+0.005} _{-0.005}	124 ⁺⁴ ₋₄
	145.54 ^{+0.01} _{-0.01}	[O I]	0.56 ^{+0.03} _{-0.03}	4.9 ^{+0.5} _{-0.4}
	157.74 ^{+0.01} _{-0.01}	[C II]	0.58 ^{+0.03} _{-0.03}	12 ⁺¹ ₋₁
G159 (Center) (<i>G159.6-18.5</i>)	157.76 ^{+0.01} _{-0.01}	[C II]	0.62 ^{+0.01} _{-0.01}	0.37 ^{+0.02} _{-0.02}
G159 (Rim)	157.76 ^{+0.01} _{-0.01}	[C II]	0.57 ^{+0.01} _{-0.01}	0.49 ^{+0.02} _{-0.02}
NGC6334 (V)	51.81 ^{+0.03} _{-0.03}	[O III]	0.38 ^{+0.09} _{-0.08}	12 ⁺⁴ ₋₄
	63.16 ^{+0.01} _{-0.01}	[O I]	0.25 ^{+0.02} _{-0.02}	13 ⁺² ₋₂
	88.38 ^{+0.02} _{-0.02}	[O III]	0.34 ^{+0.05} _{-0.05}	9 ⁺² ₋₂
	145.54 ^{+0.01} _{-0.01}	[O I]	0.54 ^{+0.01} _{-0.01}	2.21 ^{+0.08} _{-0.08}
	157.70 ^{+0.01} _{-0.01}	[C II]	0.62 ^{+0.03} _{-0.03}	10 ⁺¹ ₋₁
NGC6334 (CP)	51.83 ^{+0.01} _{-0.01}	[O III]	0.28 ^{+0.03} _{-0.03}	7 ⁺¹ ₋₁
	57.37 ^{+0.01} _{-0.01}	[N III]	0.30 ^{+0.02} _{-0.02}	4.4 ^{+0.5} _{-0.5}
	63.19 ^{+0.01} _{-0.01}	[O I]	0.28 ^{+0.003} _{-0.003}	39.0 ^{+0.7} _{-0.7}
	88.41 ^{+0.01} _{-0.01}	[O III]	0.28 ^{+0.01} _{-0.01}	4.4 ^{+0.5} _{-0.5}
	121.98 ^{+0.02} _{-0.02}	[N II]	0.65 ^{+0.03} _{-0.02}	4.4 ^{+0.3} _{-0.3}
NGC6720	145.51 ^{+0.01} _{-0.01}	[O I]	0.613 ^{+0.008} _{-0.008}	3.19 ^{+0.06} _{-0.06}
	157.72 ^{+0.01} _{-0.01}	[C II]	0.631 ^{+0.007} _{-0.007}	22.2 ^{+0.7} _{-0.7}
	51.84 ^{+0.01} _{-0.01}	[O III]	0.262 ^{+0.006} _{-0.006}	20.3 ^{+0.8} _{-0.5}
	57.34 ^{+0.01} _{-0.01}	[N III]	0.277 ^{+0.006} _{-0.007}	6.4 ^{+0.3} _{-0.3}
	63.19 ^{+0.01} _{-0.01}	[O I]	0.276 ^{+0.004} _{-0.004}	4.4 ^{+0.1} _{-0.1}
	88.38 ^{+0.01} _{-0.01}	[O III]	0.283 ^{+0.005} _{-0.005}	14.8 ^{+0.4} _{-0.4}
	88.41 ^{+0.01} _{-0.01}	[O III]	0.62 ^{+0.01} _{-0.01}	15.1 ^{+0.5} _{-0.5}
	121.96 ^{+0.01} _{-0.01}	[N II]	0.63 ^{+0.02} _{-0.02}	0.33 ^{+0.02} _{-0.02}
	145.54 ^{+0.01} _{-0.01}	[O I]	0.68 ^{+0.04} _{-0.04}	0.17 ^{+0.02} _{-0.02}
	157.76 ^{+0.01} _{-0.01}	[C II]	0.59 ^{+0.02} _{-0.02}	0.60 ^{+0.03} _{-0.02}

NOTE—Notation the same as in Table 2

Table 4. Kes 79 Raster Map 63 μm [O I] Observations

Raster	R.A. (J2000)	Decl. (J2000)	FWHM (%) ^c (μm)	Surface Brightness (10^{-4} ergs s ⁻¹ cm ⁻² sr ⁻¹)	Velocity ^a km s ⁻¹	Shift ^b (km s ⁻¹)
1	18 ^h 52 ^m 42 ^s .33	+00°39′46″.89	0.27 ^{+0.01} _{-0.01}	0.68 ^{+0.04} _{-0.04}
2	18 ^h 52 ^m 45 ^s .25	+00°40′11″.13	0.29 ^{+0.01} _{-0.01}	0.69 ^{+0.05} _{-0.05}
3	18 ^h 52 ^m 48 ^s .17	+00°40′35″.37	0.291 ^{+0.01} _{-0.01}	0.65 ^{+0.04} _{-0.04}
4	18 ^h 52 ^m 51 ^s .08	+00°40′59″.62	0.29 ^{+0.02} _{-0.01}	0.59 ^{+0.06} _{-0.06}
5	18 ^h 52 ^m 54 ^s .00	+00°41′23″.86	0.28 ^{+0.01} _{-0.01}	0.52 ^{+0.02} _{-0.02}	...	100 ⁺¹⁰ ₋₁₀

Table 4 continued

Table 4 (continued)

Raster	R.A.	Decl.	FWHM (%) ^c	Surface Brightness	Velocity ^a	Shift ^b
	(J2000)	(J2000)	(μm)	($10^{-4} \text{ ergs s}^{-1} \text{ cm}^{-2} \text{ sr}^{-1}$)	km s^{-1}	(km s^{-1})
6	18 ^h 52 ^m 56 ^s .92	+00°41'48''09	0.28 ^{+0.01} _{-0.01}	0.62 ^{+0.03} _{-0.03}	...	80 ⁺²⁰ ₋₂₀
7	18 ^h 52 ^m 59 ^s .83	+00°42'12''34	0.28 ^{+0.01} _{-0.01}	0.63 ^{+0.02} _{-0.02}	...	70 ⁺¹⁰ ₋₁₀
8	18 ^h 53 ^m 02 ^s .75	+00°42'36''58	0.31 ^{+0.01} _{-0.01}	0.71 ^{+0.03} _{-0.03}
9	18 ^h 53 ^m 05 ^s .66	+00°43'00''82	0.28 ^{+0.01} _{-0.01}	0.68 ^{+0.02} _{-0.02}	...	60 ⁺¹⁰ ₋₁₀

NOTE—Notation the same as in Table 2

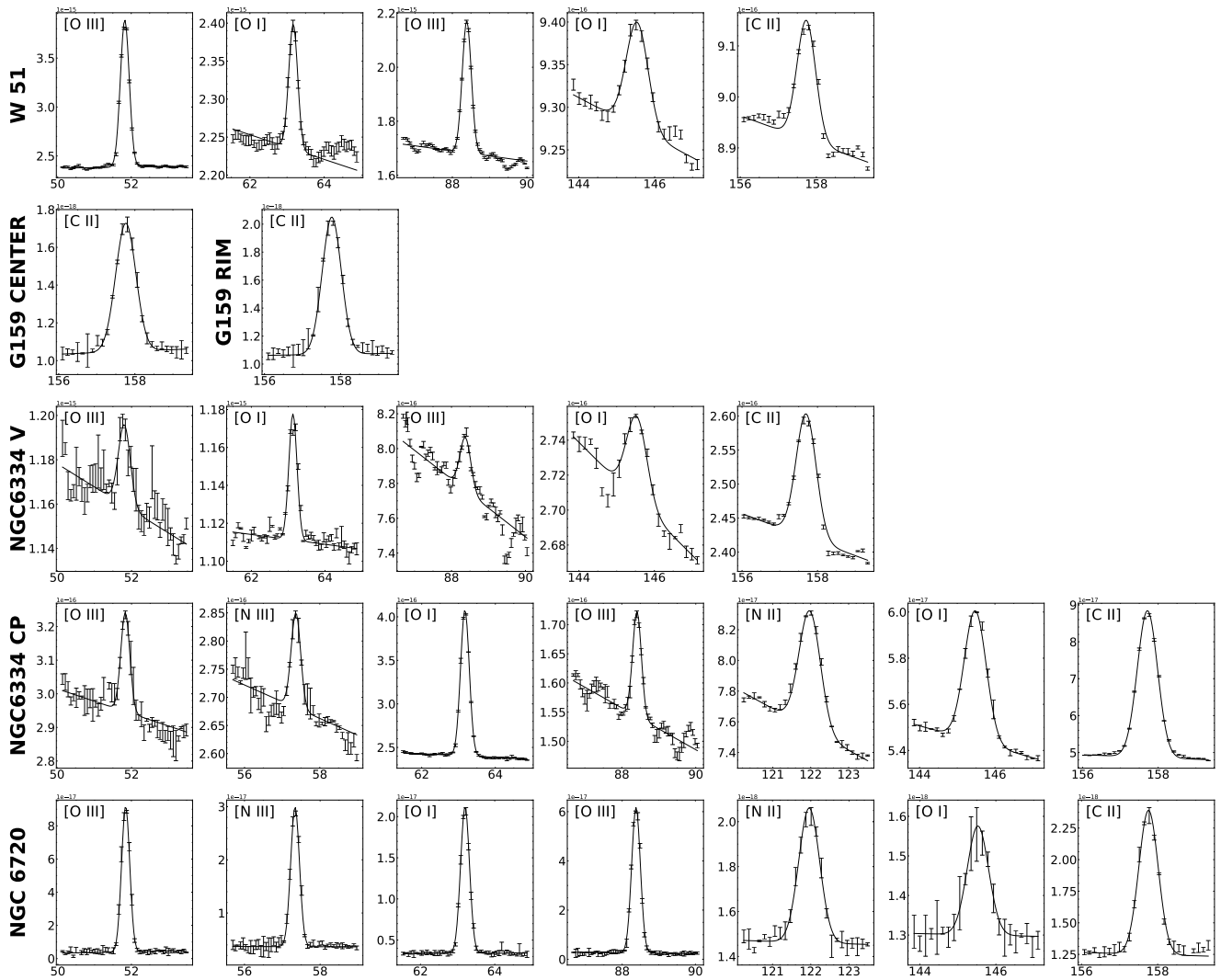


Figure 27. FIR Lines of HII Regions. Presentation is the same as Figure 26.

Table 5. CTB 109 Raster Map 63 μm [O I] Observations

Raster	R.A.	Decl.	FWHM (%) ^c	Surface Brightness	Velocity ^a	Shift ^b
	(J2000)	(J2000)	(μm)	(10^{-4} ergs s ⁻¹ cm ⁻² sr ⁻¹)	(km s ⁻¹)	(km s ⁻¹)
1	22 ^h 59 ^m 29 ^s .61	+58°50′11″.35	0.28 ^{+0.02} _{-0.03}	0.20 ^{+0.03} _{-0.04}
2	22 ^h 59 ^m 46 ^s .21	+58°52′16″.99	0.29 ^{+0.01} _{-0.01}	0.26 ^{+0.02} _{-0.02}	...	-50 ⁺¹⁰ ₋₁₀
3	23 ^h 00 ^m 02 ^s .87	+58°54′22″.51	0.39 ^{+0.06} _{-0.05} (38 ⁺²¹ ₋₁₈ %)	0.22 ^{+0.05} _{-0.05}	1300 ⁺⁴⁰⁰ ₋₄₀₀	-150 ⁺¹⁰⁰ ₋₉₀
4	23 ^h 00 ^m 19 ^s .55	+58°56′27″.89	0.27 ^{+0.03} _{-0.03}	0.14 ^{+0.02} _{-0.02}
5	23 ^h 00 ^m 36 ^s .26	+58°58′33″.14	0.24 ^{+0.03} _{-0.03}	0.09 ^{+0.02} _{-0.02}
6	23 ^h 00 ^m 53 ^s .01	+59°00′38″.25	0.27 ^{+0.06} _{-0.07}	0.12 ^{+0.04} _{-0.05}
7	23 ^h 01 ^m 09 ^s .79	+59°02′43″.22	0.24 ^{+0.08} _{-0.05}	0.12 ^{+0.08} _{-0.07}	...	-200 ⁺²⁰⁰ ₋₁₀₀
8	23 ^h 01 ^m 26 ^s .61	+59°04′48″.07	0.35 ^{+0.03} _{-0.04} (24 ⁺¹¹ ₋₁₄ %)	0.21 ^{+0.04} _{-0.04}	1000 ⁺³⁰⁰ ₋₃₀₀	...
9	23 ^h 01 ^m 43 ^s .46	+59°06′52″.77	0.48 ^{+0.09} _{-0.08} (70 ⁺³² ₋₂₈ %)	0.17 ^{+0.06} _{-0.06}	1800 ⁺⁶⁰⁰ ₋₅₀₀	...
10	23 ^h 02 ^m 00 ^s .35	+59°08′57″.34	0.37 ^{+0.13} _{-0.07} (31 ⁺⁴⁶ ₋₂₅ %)	0.17 ^{+0.08} _{-0.07}	1200 ⁺⁹⁰⁰ ₋₅₀₀	-300 ⁺¹⁰⁰ ₋₁₀₀
11	23 ^h 02 ^m 17 ^s .26	+59°11′01″.77	0.28 ^{+0.04} _{-0.04}	0.12 ^{+0.04} _{-0.04}

NOTE—Notation the same as in Table 2

Table 6. IC 443 Raster Map Observations

Raster	R.A.	Decl.	FWHM (%) ^c	Surface Brightness	Velocity ^a	Shift ^b
	(J2000)	(J2000)	(μm)	(10^{-4} ergs s ⁻¹ cm ⁻² sr ⁻¹)	(km s ⁻¹)	(km s ⁻¹)
63 μm [O I]						
1	06 ^h 16 ^m 58 ^s .52	+22°13′45″.22	0.27 ^{+0.02} _{-0.02}	0.35 ^{+0.07} _{-0.07}
2	06 ^h 17 ^m 00 ^s .78	+22°16′42″.47	0.28 ^{+0.02} _{-0.02}	0.62 ^{+0.06} _{-0.06}	...	120 ⁺⁴⁰ ₋₄₀
3	06 ^h 17 ^m 03 ^s .05	+22°19′39″.71	0.30 ^{+0.01} _{-0.01}	1.97 ^{+0.05} _{-0.05}
4	06 ^h 17 ^m 05 ^s .32	+22°22′36″.95	0.31 ^{+0.01} _{-0.01}	0.77 ^{+0.04} _{-0.04}
5	06 ^h 17 ^m 07 ^s .59	+22°25′34″.19	0.26 ^{+0.01} _{-0.01}	9.7 ^{+0.4} _{-0.4}	...	60 ⁺¹⁰ ₋₁₀
6	06 ^h 17 ^m 09 ^s .86	+22°28′31″.43	0.32 ^{+0.02} _{-0.01}	0.81 ^{+0.06} _{-0.06}
7	06 ^h 17 ^m 12 ^s .14	+22°31′28″.66	0.29 ^{+0.02} _{-0.02}	0.20 ^{+0.08} _{-0.08}	...	290 ⁺²⁰ ₋₂₀
8	06 ^h 17 ^m 14 ^s .42	+22°34′25″.89	0.22 ^{+0.03} _{-0.03}	0.48 ^{+0.08} _{-0.09}	...	160 ⁺⁸⁰ ₋₇₀
9	06 ^h 17 ^m 16 ^s .69	+22°37′23″.12	0.30 ^{+0.01} _{-0.01}	0.76 ^{+0.05} _{-0.05}	...	200 ⁺¹⁰ ₋₁₀
145 μm [O I]						
1	06 ^h 16 ^m 58 ^s .52	+22°13′45″.22	0.5 ^{+0.3} _{-0.3}	0.013 ^{+0.009} _{-0.009}
2	06 ^h 17 ^m 00 ^s .78	+22°16′42″.47	0.57 ^{+0.05} _{-0.05}	0.03 ^{+0.01} _{-0.01}	...	160 ⁺⁵⁰ ₋₄₀
3	06 ^h 17 ^m 03 ^s .05	+22°19′39″.71	0.61 ^{+0.04} _{-0.04}	0.08 ^{+0.01} _{-0.01}
4	06 ^h 17 ^m 05 ^s .32	+22°22′36″.95	0.54 ^{+0.06} _{-0.05}	0.05 ^{+0.01} _{-0.01}
5	06 ^h 17 ^m 07 ^s .59	+22°25′34″.19	0.58 ^{+0.01} _{-0.01}	0.32 ^{+0.01} _{-0.01}
6	06 ^h 17 ^m 09 ^s .86	+22°28′31″.43	0.84 ^{+0.07} _{-0.06} (43 ⁺¹² ₋₁₀ %)	0.05 ^{+0.01} _{-0.01}	1200 ⁺²⁰⁰ ₋₂₀₀	-100 ⁺⁴⁰ ₋₄₀
7	06 ^h 17 ^m 12 ^s .14	+22°31′28″.66	0.48 ^{+0.09} _{-0.07}	0.03 ^{+0.01} _{-0.01}
8	06 ^h 17 ^m 14 ^s .42	+22°34′25″.89	0.46 ^{+0.05} _{-0.05}	0.04 ^{+0.01} _{-0.01}	...	160 ⁺⁷⁰ ₋₆₀
9	06 ^h 17 ^m 16 ^s .69	+22°37′23″.12	0.62 ^{+0.05} _{-0.05}	0.05 ^{+0.01} _{-0.01}
158 μm [C II]						
1	06 ^h 16 ^m 58 ^s .52	+22°13′45″.22	0.58 ^{+0.02} _{-0.02}	0.22 ^{+0.02} _{-0.02}

Table 6 continued

Table 6 (continued)

Raster	R.A.	Decl.	FWHM (%) ^c	Surface Brightness	Velocity ^a	Shift ^b
	(J2000)	(J2000)	(μm)	(10^{-4} ergs s ⁻¹ cm ⁻² sr ⁻¹)	(km s ⁻¹)	(km s ⁻¹)
2	06 ^h 17 ^m 00 ^s .78	+22° 16′ 42″.47	0.59 ^{+0.04} _{-0.04}	0.36 ^{+0.04} _{-0.04}
3	06 ^h 17 ^m 03 ^s .05	+22° 19′ 39″.71	0.60 ^{+0.02} _{-0.02}	0.77 ^{+0.06} _{-0.06}
4	06 ^h 17 ^m 05 ^s .32	+22° 22′ 36″.95	0.54 ^{+0.04} _{-0.04}	0.49 ^{+0.06} _{-0.05}
5	06 ^h 17 ^m 07 ^s .59	+22° 25′ 34″.19	0.60 ^{+0.02} _{-0.02}	1.37 ^{+0.04} _{-0.04}
6	06 ^h 17 ^m 09 ^s .86	+22° 28′ 31″.43	0.62 ^{+0.02} _{-0.02}	0.41 ^{+0.02} _{-0.02}
7	06 ^h 17 ^m 12 ^s .14	+22° 31′ 28″.66	0.58 ^{+0.04} _{-0.03}	0.27 ^{+0.03} _{-0.03}	...	70 ⁺³⁰ ₋₂₀
8	06 ^h 17 ^m 14 ^s .42	+22° 34′ 25″.89	0.63 ^{+0.02} _{-0.02}	0.39 ^{+0.04} _{-0.04}	...	70 ⁺³⁰ ₋₃₀
9	06 ^h 17 ^m 16 ^s .69	+22° 37′ 23″.12	0.4 ^{+0.1} _{-0.2}	0.3 ^{+0.2} _{-0.2}

NOTE—Notation the same as in Table 2

3. DETECTED LINE PROFILES

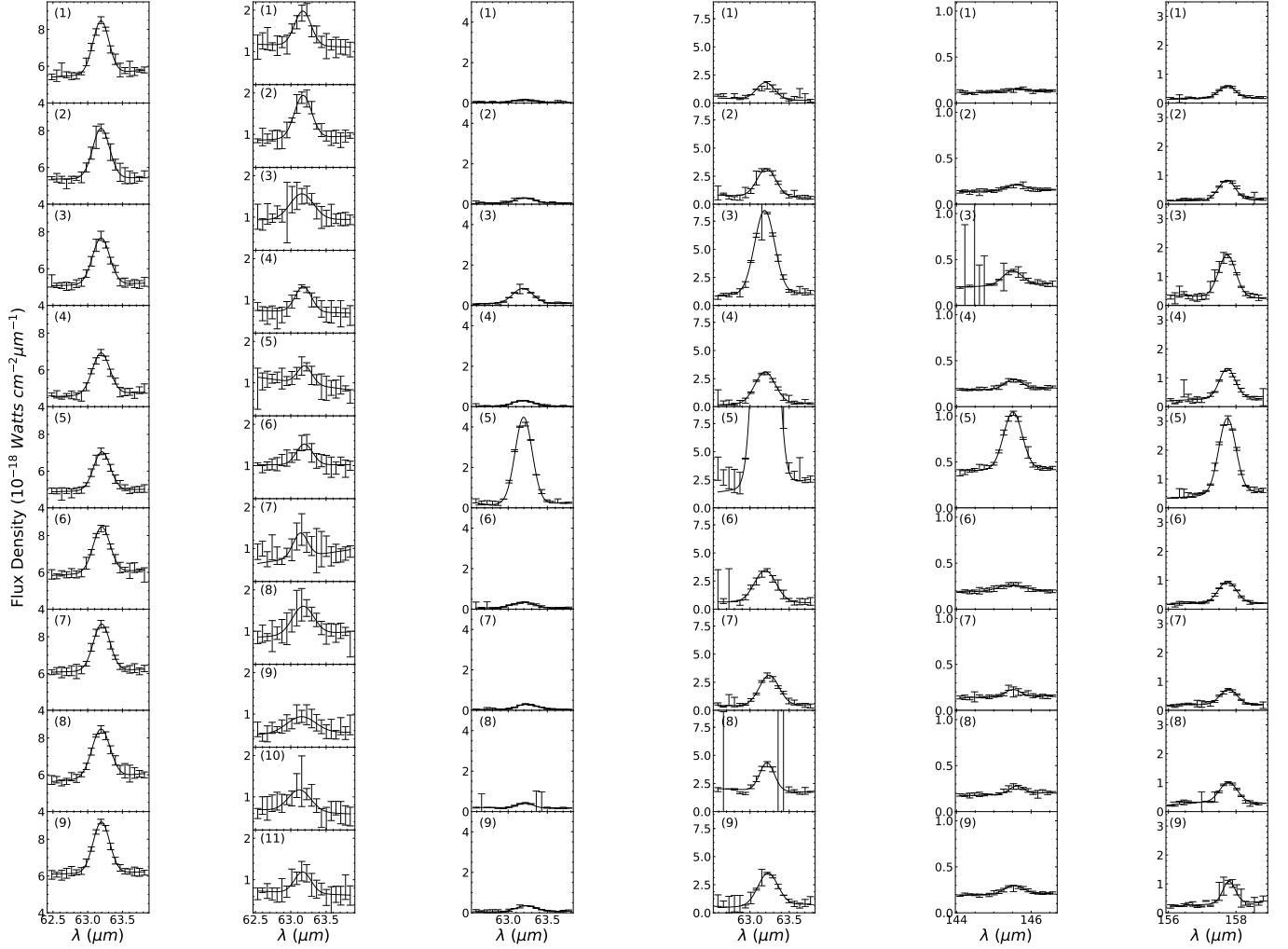
The candidate atomic fine-structure emission lines are approximately Gaussian in shape and the underlying continuum is roughly linear over small wavelength ranges. Thus, we fit the narrow-band spectrum of each line with a Gaussian + linear component model (Levenberg–Marquardt algorithm) using the Python package “LMFIT” (Newville et al. 2014). These narrow-band line spectra and best-fit models are plotted in Figure 26, and our results are summarized in Table 2. We clearly detect atomic fine-structure emission lines from [C II] at 158 μm , [N II] at 122 μm , [O I] at 63 and 145 μm , and [O III] at 52 and 88 μm in several remnants. On several occasions, the [O I] 63 and 145 μm and [O III] 88 μm lines are detected in adjacent subdetectors. The SW3 subdetector always covers the [O I] 63 μm band, while its adjacent subdetector (SW2) covers this band only in a few observations. For the [O I] 145 μm line, while both the LW3 and LW4 subdetectors always cover the wavelength band of interest, LW4 consistently provides better signal-to-noise (S/N). The [O III] 88 μm line is detected with both the SW5 and LW1 detectors. The SW5 detector provides roughly twice the resolving power of LW1 (Table 7). Therefore, we report the [O I] 63 and 145 μm and [O III] 88 μm line measurements detected with the SW3, LW4, and SW5 subdetectors, respectively. In a few cases, the data quality is poor in these detectors, so we instead report measurements using the adjacent subdetector. We note these exceptions in Table 2.

A clear signature of emission lines emanating from fast-moving ejecta gas from a SN is their significant Doppler broadening, which may be detected in the *ISO* LWS spectra of SNRs. To calculate the velocity broadening (B) of each emission line, we remove the effect of the instrumental broadening through the relation,

$B_{Line} = \sqrt{B_{Obs}^2 - B_{LWS}^2}$, where B_{Obs} is the observed full width at half maximum (FWHM) of the emission line, B_{LWS} is the instrument resolution of the LWS detector (Table 7), and B_{Line} is the true FWHM of the line. We measure an apparent Doppler broadening of $B_{Line} \gtrsim 1000$ km s⁻¹ for several emission lines, mostly from the 63 μm [O I] and 88 μm [O III] lines (see Figure 29 and Table 8). The detection of [C II] lines requires caution because [C II] 158 μm emission is the primary coolant in interstellar gas. Galactic plane surveys of the [C II] 158 μm line revealed ambient intensities of $\sim 10^{-5} - 10^{-4}$ erg s⁻¹ cm⁻² sr⁻¹ (Bennett et al. 1994; Nakagawa et al. 1998; Pineda et al. 2013). Thus, our measured line profiles may be contaminated by emissions originating from along the line-of-sight, not associated with the SNR. Unfortunately, in most cases, no accompanying background observation is available to distinguish between the line-of-sight and SNR emission. Future on-off observations are required to unambiguously determine if the [C II] emission belongs to the SNR. Nonetheless, a clear case of Doppler-broadening of the [C II] 158 μm line is in the Crab Nebula ($B_{Line} \sim 1800$ km s⁻¹). We also note that the *Herschel* spectroscopic observation of Kes 75 (G29.7-0.3) resolves the [C II] line into two components of narrow and broad (1300 – 1500 km s⁻¹) (Temim et al. 2019), while the *ISO* spectra indicate 8% broadening of this [C II] line. The *Herschel* Photodetector Array Camera and Spectrometer (PACS) resolution (~ 240 km s⁻¹) at 158 μm is a factor of ~ 5 superior to that of the *ISO* LWS (~ 1100 km s⁻¹). The marginally detected broadening of the [C II] line in the LWS spectra may need to be verified (or disputed) by future follow-up observations.

4. HIGH VELOCITY SN EJECTA

We compared our measured FWHM values for the detected emission lines with the instrumental FWHM reported in the *ISO* LWS Handbook, ~ 0.283 μm and \sim



(a) Kes 79: 63 μm (b) CTB 109: 63 μm (c) IC 443: 63 μm (d) Same as (c) Zoomed (e) IC 443: 145 μm (f) IC 443: 158 μm

Figure 28. FIR Lines of LWS Observations with multiple raster pointings.

Table 7. Spectral Resolution of *ISO* LWS

Detector	Line	Detector FWHM ^a		NGC 6720 FWHM	
		(μm)	(km s^{-1})	(μm)	(km s^{-1})
SW2 (49.5–64 μm)	52 μm ([O III])	0.283 \pm 0.009	1640 \pm 50	0.262 \pm 0.006	1510 \pm 40
SW3 (57–70 μm)	57 μm ([N III])	0.283 \pm 0.009	1480 \pm 50	0.277 \pm 0.007	1450 \pm 40
SW3	63 μm ([O I])	0.283 \pm 0.009	1400 \pm 40	0.283 \pm 0.003	1400 \pm 20
SW5 (76–93 μm)	88 μm ([O III])	0.283 \pm 0.009	1340 \pm 40	0.283 \pm 0.005	1340 \pm 20
LW1 (84–110 μm)	88 μm ([O III])	0.584 \pm 0.015	1980 \pm 50	0.618 \pm 0.013	2100 \pm 40
LW2 (103–128 μm)	122 μm ([N II])	0.584 \pm 0.015	1440 \pm 40	0.634 \pm 0.024	1560 \pm 60
LW4 (142–171 μm)	145 μm ([O I])	0.584 \pm 0.015	1200 \pm 30	0.680 \pm 0.044	1400 \pm 90
LW4	158 μm ([C II])	0.584 \pm 0.015	1100 \pm 30	0.599 \pm 0.016	1140 \pm 30

^a*ISO* LWS Handbook (Gry et al. 2003)

0.584 μm for lines detected with the SW and LW sub-detectors (see Table 7, respectively (Gry et al. 2003). We note that these instrumental resolutions are consistent (within statistical uncertainties) with the line width measurements for our HII region sample and the planetary nebula NGC 6720 (see Table 3). For each emission line, we take the instrumental FWHM (B_{LWS}) to be the smaller value of either the FWHM reported in the *ISO* LWS Handbook or our measured FWHM of the emission line in NGC 6720 (Table 7). Note that the handbook provides only one number for each of SW and LW and the FWHM is expected to be a function of wavelength because the LWS is a grating instrument. We confirm that using either the *ISO* Handbook or our measured NGC 6720 values for the detector resolutions does not significantly affect our scientific conclusions.

We detect broad lines (up to $\sim 3000 \text{ km s}^{-1}$) in several SNRs including G21.5–0.9, G29.7–0.3, the Crab Nebula, and G320.4–1.2. The velocity profiles of a few representative cases are shown in Figure 29. We classify these SNRs into three groups based on the statistical significance of the measured intensity and broadening of at least one emission line in each SNR spectrum: i.e., – Group A: both a firm line detection with $S/N > 5$ and a clear 5σ broadening detection, Group B: the line is firmly detected ($S/N > 5$), but the broadening is marginal ($< 5 \sigma$), and Group C: the lines appear to be broad, but the line detection is marginal ($3 < S/N < 5$), or show a marginal broadening only in the [C II] 158 μm line. In Table 8, we summarize these results.

The spectrum of the Crab Nebula (see Figure 29) shows clear evidence of broad emission lines from high-speed ejecta. Its spectrum exhibits double-peaked line features (Figure 26, [O III] 88 μm), indicating both blue- and red-shifted emission components expanding along the line of sight. In fact, all detected emission lines (i.e., 52 and 88 μm [O III], 63 and 145 μm [O I], 122 μm [N II], and 158 μm [C II]) from its spectra are broad, with line widths of $B_{Line} \sim 2000\text{--}3000 \text{ km s}^{-1}$. The 88 μm [O III] line in G320.4–1.2 shows an asymmetrical broadening, which may also suggest double-peaks with differential blue and red shifts (Figure 29). Below, we discuss individual SNRs with evidence of ejecta emission in detail.

G21.5–0.9 – Observations of the PWN with the *Herschel* PACS detector revealed broad [O I] 63 μm and [C II] 158 μm lines with measured FWHMs of 850 km s^{-1} and 1000 km s^{-1} , respectively, indicating the presence of PWN-shocked ejecta (Hattori et al. 2020; Cha et al. 2021). The LWS pointing encompasses almost all of the IR emission of the PWN (see Figure 4). The FIR lines at 63 μm [O I], 122 μm [N II], and 145 μm [O I] show broadening (Table 2, Figure 26). The broadening

at 63 μm is firmly detected, thus we classify the detection into Group A, indicating that the emission likely originates from fast-moving ejecta. Our estimates of the [O I] 63 μm and 145 μm line FWHMs of $\sim 900 \text{ km s}^{-1}$, are consistent with the measured values from the *Herschel* PACS observations.

G29.7–0.3 – *Herschel* PACS observations of the PWN showed narrow and broad components for each of the [O I] 63 μm , [O III] 88 μm , and [C II] 158 μm emission lines (Temim et al. 2019). Temim et al. (2019) attributed the narrow component to background emission, and estimated FWHMs of 1270 – 1570 km s^{-1} for the broad components, suggesting that the PWN shock is interacting with ejecta in the interior of the remnant.

The *ISO* LWS pointing covers the entirety of the PWN as seen in the FIR (Figure 5). We detect broad [N II] 122 μm and [O I] 145 μm lines. The broadening is firmly detected for the [N II] 122 μm (1200 km s^{-1}) and [O I] 145 μm (1300 km s^{-1}) lines (Group A). This is the first detection of [O I] 145 and [N II] 122 μm line broadening in this SNR. Our measured line widths are consistent with those detected at [O I] 63 and [O III] 88 μm based on the *Herschel* PACS data Temim et al. (2019).

G54.1+0.3 – Temim et al. (2010) suggested that the IR morphology is due to the PWN driving shocks into the expanding SN ejecta. Using *Spitzer* archival IRS, IRAC, and MIPS data, Rho et al. (2018) found dust emission spatially coincident with the ejecta line emission as traced by [Ar II]. In addition to Ar, they also detected atomic fine-structure emission from Ne, Cl, Si, and S. These lines are broadened, corresponding to velocities up to several 10^2 km s^{-1} . The [C II] line at 158 μm shows a slight, but statistically significant ($> 5 \sigma$) broadening of $B_{Line} = 640 \text{ km s}^{-1}$. However, the [C II] emission contribution from the remnant is unclear due to contamination from line-of-sight emission. Thus, we classify this SNR as Group C.

Crab Nebula – Gomez et al. (2012) showed that broad atomic lines observed with the *ISO* LWS correspond with resolved redshifted and blueshifted emission peaks in the *Herschel* PACS spectra from a bright filament at the eastern side of the remnant. With the higher-resolution PACS data, they estimate that the redshifted and blueshifted emission peaks are in the velocity range of 1290 – 1750 km s^{-1} .

Here, our results are based on a pointing toward the northern part of the remnant (Figure 11). The [O III] 52 and 88 μm , [N III] 57 μm , [O I] 63 and 145 μm , [N II] 122 μm , and [C II] 158 μm lines are broad ($\sim 1800\text{--}3300 \text{ km s}^{-1}$, Table 2). The double-peaked structure due to red- and blue-shifted components is resolved in

the LWS data for the [O III] 88 μm line (Figure 26). Applying a two-Gaussian + linear component model fit to this line gives line centroid values corresponding to

$\pm 1000 \text{ km s}^{-1}$. The Crab Nebula exhibits the clearest case in our sample of broad line emission originating from high-speed ejecta.

Table 8. Properties of Young SNRs with Broad FIR Lines

SNR	Distance	Age	M_{dust}	Progenitor	Broad Lines ^a	Measured ^a	Group	52/88 μm^a	63/145 μm^a
	(kpc)	(yr)	<i>Herschel</i> (M_{\odot})	Mass (M_{\odot})	(μm)	FWHM(km s^{-1})			
G21.5–0.9	4.8 ¹	<1000 ^{2,3}	0.29 ⁴	–	63,122,145	900–1800	A	–	11
G29.7–0.3	5.1–10.6 ^{5,6}	723 ⁷	0.51 ⁴	8–12 ⁸	122,145	1200–1300	A	–	1.3
G54.1+0.3	6.2 ¹⁶	1800–2400 ¹⁷	0.08–0.9 ¹⁸	15–20 ¹⁹	158	640	C	–	–
Crab Nebula	2 ⁹	966	0.016–0.6 ^{10–13}	8–10 ¹⁴	51,63,88,122,145,158	1800–3300	A	1.4, 1.0 ^b	17
G320.4–1.2	5.2 ¹⁵	1700 ¹⁵	^e 0.009	–	88,122	1800–2100	A	–	–
RCW 103	3.1 ²⁰	2000 ²¹	0.18 ²² , 1.1 ²³	18–20 ²⁴	63,122	800–2000	C	–	6.1, 15 ^c
E0102.2–7219	61	2050 ²⁵	^e 0.014 ²⁶	25 – 40 ^{27,28,39}	88	1300	C	–	–
N132D	50	2500 ²⁹	^d 0.013 ³⁰	15 \pm 5 ³¹	63	1500	B	–	–
N49	50	4800 ³²	\geq 0.1 ³³	13 – 17 ³⁴	88	3000	C	–	–
0540–69.3	50	800 – 1100 ³⁵	^{d,e} 1 – 3 \times 10 ^{–3} ^{36,37}	20 – 25 ³⁸	52	2900	C	4.5	–

NOTE—1. Tian & Leahy (2008) 2. Guest et al. (2019) 3. Bietenholz & Bartel (2008) 4. Chawner et al. (2019) 5. Leahy & Tian (2008) 6. Su et al. (2009) 7. Gotthelf et al. (2000) 8. Temim et al. (2019) 9. Trimble (1968) 10. De Looze et al. (2019) 11. Gomez et al. (2012) 12. Temim & Dwek (2013) 13. Owen & Barlow (2015) 14. Smith (2013) 15. Gaensler et al. (1999) 16. Leahy et al. (2008) 17. Bocchino et al. (2010) 18. Rho et al. (2018) 19. Gelfand et al. (2015) 20. Reynoso et al. (2004) 21. Carter et al. (1997) 22. Pinheiro Gonçalves et al. (2011) 23. Andersen et al. (2011) 24. Frank et al. (2015) 25. Finkelstein et al. (2006) 26. Rho et al. (2009) 27. Blair et al. (2000) 28. Flanagan et al. (2004) 29. Law et al. (2020) 30. Seok et al. (2008) 31. Sharda et al. (2020) 32. Park et al. (2012) 33. Otsuka et al. (2010) 34. Zhou et al. (2019) 35. Reynolds (1985) 36. Williams et al. (2008) 37. Lundqvist et al. (2020) 38. (Lundqvist et al. 2011) 39. Alan et al. (2019)

^aThis work (*ISO* LWS). ^bBlue, red-shifted line ^cCenter, rim ^d*AKARI* estimate ^e*Spitzer* estimate
Group A: Line flux and line broadening are both significant to $\geq 5\sigma$; Group B: Significance of broad line emission is $> 5\sigma$, line broadening significance is $< 5\sigma$; Group C: Significance of broad line flux $< 5\sigma$.

G320.4–1.2 – Koo et al. (2011) reported a clump of gas near the PWN emitting a [Ne II] 12.81 μm line with a line-of-sight velocity of $\sim +1000 \text{ km s}^{-1}$, indicating SN ejecta. A recent X-ray proper motion study of compact ejecta knots located to the north of the pulsar (in the RCW 89 nebula) indicates high velocities up to 5000 km s^{-1} (Borkowski et al. 2020).

The LWS pointing is centered on the PWN, which shows a complicated structure of filaments in the *Herschel* 70 μm image (Figure 32). We detect [O I] 63 μm , [O III] 88 μm , [N II] 122 μm , and [C II] 158 μm emission lines. The 88 μm [O III] is broadened by $\sim 2000 \text{ km s}^{-1}$ (Group A). Our detection of broad lines is consistent with similar high-speed ejecta emission reported in Koo et al. (2011) and Borkowski et al. (2020). G320.4–1.2 shows promising evidence for emission from both ejecta and dust from the same region (see Section 6 for a detailed discussion of the continuum emission).

RCW 103 – A previous *ISO* study found that the post-shock gas has low densities ($n_e \sim 10^3 \text{ cm}^{-3}$) and abundances close to solar values, and thus no clear indication of ejecta emission (Oliva et al. 1999). A *Chandra* study found sparse ejecta emission throughout SNR, with abundance values slightly above solar values (Frank et al. 2015).

We examined the *ISO* LWS spectra of two sub-regions within RCW 103, one near the SNR’s center and the other at the bright southern shell (regions # 1 and # 3, respectively, see Figure 15). We extracted the back-

ground spectrum from another LWS data pointed at a region just outside of the southern shell of RCW 103 (region # 2, Figure 15). We find that the region # 3 spectrum clearly shows enhanced [O I] line emission at 63 μm above the background spectrum (see Table 2), which may be related to shock interactions with a molecular cloud (see Section 5). The central region (# 1) shows marginal evidence for line-broadening, however the line strengths are similar to (or even weaker than) those measured in the background region. Thus, the line-broadening is not compelling, and we classify this SNR as Group C.

E0102.2–7219 – Optical observations suggest the presence of fast-moving ejecta emitting [S II], [S III], [Ar III], and H α and H β lines at speeds up to $\sim 1800 \text{ km s}^{-1}$ (Seitenzahl et al. 2018). Rho et al. (2009) measured several MIR emission lines from ejecta, including broad [Ne III] and [Ne V] lines which suggest velocity dispersion ranges of $\sim 2000 - 4000 \text{ km s}^{-1}$.

We measure a candidate broad [O III] 88 μm line, suggesting a velocity up to $\sim 1300 \text{ km s}^{-1}$. However, the broadening is statistically insignificant ($\sim 1 \sigma$), and the line detection is marginal ($\sim 4 \sigma$, Table 2). Thus, we classify this evidence into Group C.

N132D – Based on *Spitzer* IRS, IRAC, and MIPS data, Tappe et al. (2012) detected [Ne II] and [O IV] MIR lines from a fast-moving ejecta knot position, while the southeastern shell is dominated by ISM (Tappe et al. 2006). We detect the [O I] 63 μm and 145 μm lines. The [O I] 63 μm line appears to be broadened (a 3 σ

detection, Group B). The implied velocity dispersion is $\sim 1500 \text{ km s}^{-1}$. If our suggested line broadening would be confirmed with follow-up observations, this velocity would be in plausible agreement with kinematic studies of the optical [O III] ejecta which estimate expansion velocities up to $\sim 3000 \text{ km s}^{-1}$ (Morse et al. 1995; Law et al. 2020).

N49 – Bilikova et al. (2007) estimated regional expansion velocities up to $\sim 500 \text{ km s}^{-1}$ based on echelle spectra of H α and [N II] emission lines, while X-ray observations indicate that N49 is enriched in Si and S (Park et al. 2003, 2012), as well as O and Ne (Zhou et al. 2019). We find marginal evidence for a broad [O III] 88 μm line (a 3 σ detection, Group C, Table 2). If confirmed, this broad [O III] line may be associated with the O-rich ejecta in this SNR.

0540-69.3 – Optical [O III] emission lines with velocity dispersions of $\sim 3000 \text{ km s}^{-1}$ have been detected in 0540-69.3 (Mathewson et al. 1980; Kirshner et al. 1989). X-ray measurements hint at metal-rich ejecta in the southern part of the SNR (Park et al. 2010). Our best-fit to the [O III] 52 μm line suggests potential broadening ($\sim 2900 \text{ km s}^{-1}$). However, the line intensity and broadening are both measured with only 3 σ confidence (Group C). The line-center is also shifted by $+1300 \text{ km s}^{-1}$, however, this shift is not detected in the [O III] 88 μm line.

Follow-up observations with higher spectral resolution (e.g., the FIFI-LS on board *SOFIA*, or the proposed *Origins* Space Telescope (Leisawitz et al. 2021)) are required to firmly detect the candidate broad lines in G54.1+0.3, RCW 103, E0102.2-7219, N132D, N49, and 0540-69.3. Furthermore, due to the large aperture (diameter = 80'') of the LWS, constructing a detailed spatial distribution of ejecta emission in SNRs of our sample is not feasible. Establishing the spatial associations between ejecta and dust emission features based on high-resolution imaging is necessary to test the dust formation in the SN ejecta.

5. SNRS INTERACTING WITH MOLECULAR CLOUDS

5.1. Diagnostic Line Results

Progenitors of CC-SN burn through their fuel in relatively short time periods, and therefore their SNRs may interact with the molecular clouds (MCs) where they were born. The high expansion speed of the SNR drives a shock into the interacting MC. The radiative cooling of the shocked gas produces a number of molecular and atomic emission lines in IR bands.

The [O I] 63 μm and 145 μm , and [C II] 158 μm line strengths are useful diagnostics for the pre-shock density

of the cloud and the speed of the shock that it encounters (Hollenbach & McKee 1989). In general, two types of shock interactions are considered, i.e., a continuous (C)-type, or jump (J)-type shock. In a C-type shock, the shock front moves at a speed slower than the magnetosonic speed in the medium, and thus the gas conditions (e.g., temperature and density) change gradually. In a J-type shock, the shock front moves faster than the magnetosonic speed, and there is a sharp change in the gas temperature and density as the shock front moves through the medium. The type of shock affects the post-shock chemistry and overall dust destruction. Here, we aim to identify shock types from our measurements of FIR [O I] and [C II] lines in these MC-interacting SNRs.

Our sample includes SNRs W 28, IC 443, Kes 79, CTB 109, and RCW 103, for which the shock-MC interaction has been reported in literature (Tatematsu et al. 1990; Dickman et al. 1992; Rho & Petre 1997; Arikawa et al. 1999; Stanimirović et al. 2003; Paron et al. 2006; Kilpatrick et al. 2016; Zhou et al. 2016). For SNRs Kes 79, CTB 109, and IC 443, the [O I] 63 μm band was observed with a raster map across the face of remnant. The raster maps allow for measurements of spatial variations in line strength across the remnant, whereby the locations of various shocks can be identified. These raster map observations focus on narrow wavelength ranges of select emission lines, not covering the full range of the LWS. The raster maps of IC 443 also include spectra of the [O I] 145 μm and [C II] 158 μm bands. The raster map narrow-band line spectra and our spectral model fits are shown in Figure 28, while Tables 4, 5, and 6 show the line profiles and best-fit results for Kes 79, CTB 109, and IC 443, respectively. Figure 30 shows the radial distribution of line intensity for each of the raster observations of the molecular-cloud interacting SNRs in our sample. In Figure 30, we also overlay the published radial distribution of the [O I] 63 μm line intensity across the northeastern shell of IC 443 (Rho et al. 2001).

The raster map of Kes 79 consists of 9 observations, each separated by 1 arcmin, which extend across the eastern boundary (see Figure 6) of the remnant. The [O I] 63 μm line intensities are consistent with the mean, $I_{63\mu\text{m}} = 6.4 \times 10^{-5} \text{ erg s}^{-1} \text{ cm}^{-2} \text{ sr}^{-1}$), to within 3 σ uncertainties. Thus, there is no clear emission enhancement between regions inside the boundary of the remnant versus outside of it.

The CTB 109 raster map (see Figure 8) consists of 11 observations positioned across the northwest quadrant of the remnant, with 3 arcmin spacing between each pointing. We note the lowest line fluxes in regions 5 — 7 located inside the boundary of the remnant, and highest near of the western perimeter. The dimmer regions

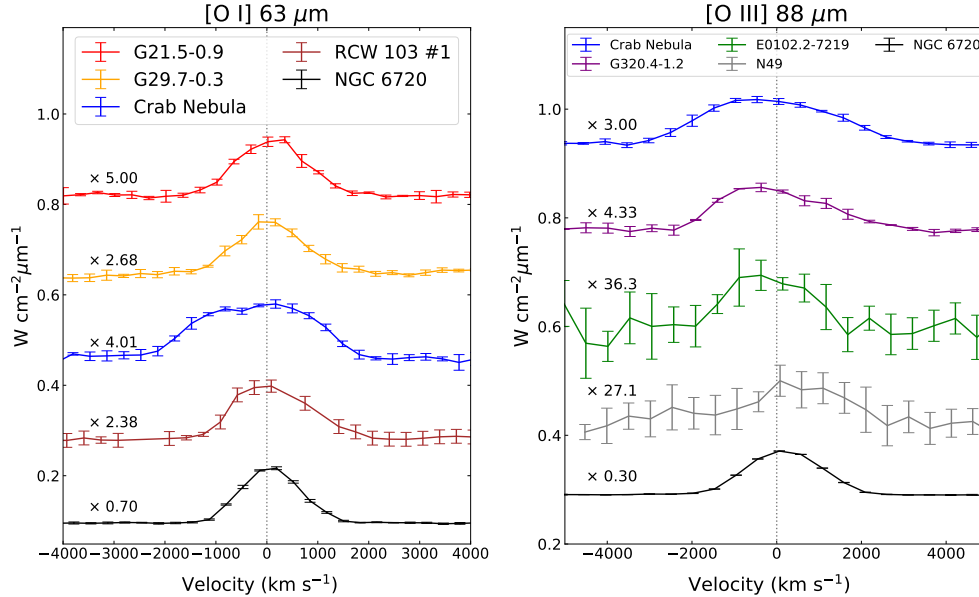


Figure 29. *ISO* LWS velocity profiles of apparently broad 63 μm [O I] and 88 μm [O III] SNR emission lines. The profiles are scaled by the value listed above each line, and shifted for comparison. The solid black line shows the profile of planetary nebula NGC 6720, which represents the velocity resolution of the detector.

roughly coincide with the location of a CO arm that reaches across the remnant (Kothes et al. 2002), which could indicate that the emission is being absorbed by a foreground MC.

The raster map of IC 443 consists of 9 observations spaced 3 arcmin apart, from the geometric center of the remnant to outside the southern shell (see Figures 12 and 30:Upper). The [O I] 63 μm , 145 μm and [C II] 158 μm lines are strongest at a bright IR ridge in the southern shell (position 5), $I_{63\mu\text{m}} = 9.7 \pm 0.4 \times 10^{-4} \text{ erg s}^{-1} \text{ cm}^{-2} \text{ sr}^{-1}$, and weakest at the position exterior to the boundary of the remnant (position 1), $I_{63\mu\text{m}} = 0.35 \pm 0.07 \times 10^{-4} \text{ cm}^{-2} \text{ s}^{-1} \text{ sr}^{-1}$. The [O I] emission peaks at the southern shell (more than an order of magnitude higher than the background intensity), indicating significant cooling from the SNR shocks encountering dense MCs. Similar sharp increases in line intensity are present in LWS observations of W44 and 3C391 (Reach & Rho 1996). IC 443 was also observed using single (non-raster) pointings directed at the southeastern (# 1), eastern (# 2), and western (# 3) boundaries of the remnant (see Table 2). The strongest [O I] and [C II] emission is observed at the southeast position. We note that [N II] lines from IC 443 show somewhat high velocity (2000 – 3000 km s^{-1}), but the significance of the detection is less than 5σ . Higher resolution spectroscopy is required to resolve if the [N II] lines are truly broad.

RCW 103 and W 28 were observed with non-raster LWS pointings. RCW 103 is close to the Galactic plane ($b = -0.4^\circ$). After background subtraction using a sepa-

rate background pointing (# 2), nearly all of the [C II] is removed from the central (# 1) and southern border (# 3) spectra (see Figure 15). At the central region, the [O I] line strength is also reduced significantly. However, at the southern ridge the [O I] flux remains high, $I_{63\mu\text{m}} = 3.7_{-0.5}^{+0.5} \times 10^{-4} \text{ erg s}^{-1} \text{ cm}^{-2} \text{ sr}^{-1}$. We note that the background emission around RCW 103 is non-uniform with a complex morphology, which may imply a significant spatial variation in the background intensity. Thus, our estimated background-subtracted flux of the [O I] line should be considered with caution. For W 28, there is no background observation. Since it is located close to the Galactic plane ($b = -0.1^\circ$), the observed line intensity may be mixed with a significant amount of line-of-sight emission.

5.2. SNR–MC Interactions and Shock Models

Below we briefly overview previously documented evidence of MC interactions for the relevant SNRs in our sample, and discuss our results for each remnant. Our estimated shock conditions based on the [O I] and [C II] emission for each of the MC-interacting SNRs are listed in Table 9 and the observed line fluxes are compared with shock models in Figure 31.

IC 443 – The MC interactions with IC 443 have been well studied. Shocked molecular gas was first detected toward the southern region of IC 443 with CO(1–0) observations that showed 20 km s^{-1} line widths (Denoyer 1979). Since then, several different molecular species have been used as tracers to study the shock-cloud interactions in the SNR (Burton et al. 1988; Dickman et al.

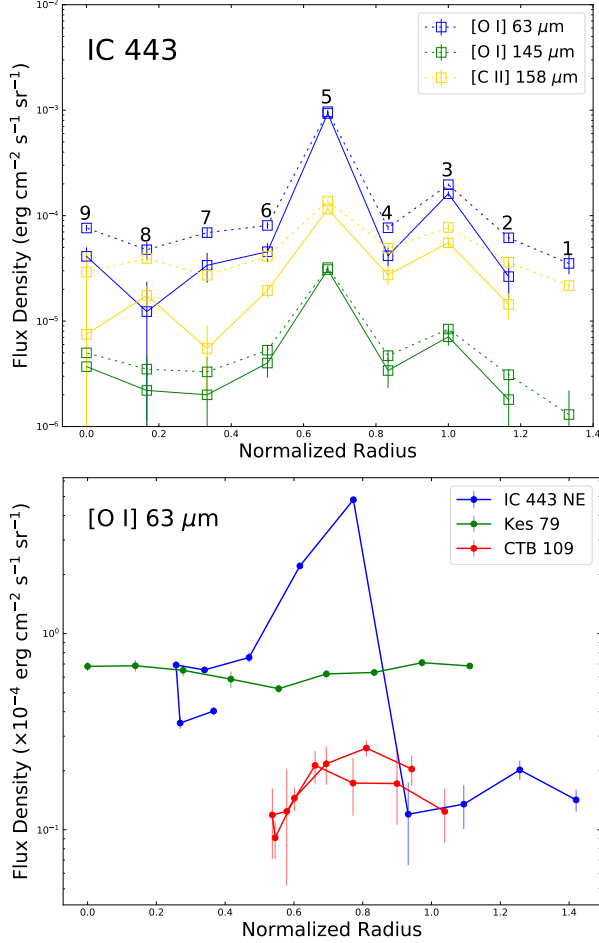


Figure 30. Upper: Distribution of [O I] and [C II] line intensity in the southern region of IC 443 (see Figure 12) as a function of distance from the center of the SNR. The total flux density in each region is represented by dashed lines, while solid lines indicate the background-subtracted values. The emission peaks at the double shell (position 5 at $r=0.7$ and 3 at $r=1.0$). Lower: Total [O I] 63 μm line intensity vs. radius for raster observations of Kes 79, CTB 109, and the northeast region of IC 443 from Rho et al. (2001) are compared with those of the southern region of IC 443 from the upper panel.

1992; van Dishoeck et al. 1993; Snell et al. 2005; Reach et al. 2019; Kokusho et al. 2020). The importance of the FIR 63 μm line of [O I] as a shock diagnostic tool was demonstrated using an observation from the Kuiper Airborne Observatory, where the [O I] emission was found to correlate well with the near-IR H_2 emission (Burton et al. 1990). The [O I] 63 μm line strength was also used to determine the nature of the shocked gas in the northeast (Rho et al. 2001). Rho et al. (2001) observed IC 443 with *ISO* LWS raster line spectra across the northeastern rim of the remnant and reported similar peak [O I] 63 μm line brightness values ($\sim 5 \times 10^{-4} \text{ erg s}^{-1} \text{ cm}^{-2} \text{ sr}^{-1}$)

to ours. Based on strong 2MASS K_s -band emission (associated with H_2 line emission) relative to the J and H bands, they suggested that the southern shell is dominated by a slow continuous C-shock, with a shock speed $v_s \sim 30 \text{ km s}^{-1}$ and preshock hydrogen density, $n_o \sim 10^4 \text{ cm}^{-3}$ (as also concluded by Cesarsky et al. (1999)).

We compare our observed line brightness with C- and J-shock models. We reproduce the J-shock model calculations of line fluxes based on Figure 7 of Hollenbach & McKee (1989)². For the C-shock models, we run the Paris-Durham code (Godard et al. 2019)³ and produce the predicted line intensities depending on density and shock velocities. We overview the Paris-Durham code in Appendix B, and present our input parameters in Table B.1. Our C-shock models assume a young shock age of 10^3 years, while the J-shock models assume the shock has reached a steady-state. Increasing the shock age of the C-shock models to 10^4 years (nearly reaching a steady-state) enhances the predicted [O I] and [C II] intensities by a factor of a few, but does not affect our conclusions. Figure 31 shows the calculated line intensities for various preshock densities ($10^3 - 10^6 \text{ cm}^{-3}$) and shock speeds ($5 - 150 \text{ km s}^{-1}$) for C-shock and J-shock models.

Our observed [O I] line brightness values in IC 443 are consistent with the lower density (10^3 cm^{-3}) fast (80 km s^{-1}) J-shock models from Hollenbach & McKee (1989). However, when we account for the large beam of the *ISO* LWS the true surface brightness may be a factor of a few smaller than the observed brightness. In this case, we find that a C-shock solution for the higher density ($10^5 - 10^6 \text{ cm}^{-3}$) and slow (30 or 10 km s^{-1}) shock models from the Paris-Durham code fits our measured [O I] line flux. The observed [C II] 158 μm line emission can be reproduced only in the fast J-shock models, suggesting that at least some of the observed emission is due to this type of shock. It is difficult to firmly constrain the nature of the shock-cloud interaction in IC 443, and the presence of multiple shocks in the SNR is often invoked (see Snell et al. (2005) for a comprehensive review of possible shock-types). Recent IR line maps of IC 443 show that H_2 line emission (indicative of slower shocks) is mainly distributed along the southern ridge, while [Fe II] emission (representative of faster shocks) is present throughout the entire remnant (Kokusho et al. 2020). Thus, both slow shocks moving into a dense gas and fast shocks into a thinner gas may be present within

²<https://automeris.io/WebPlotDigitizer/>

³<https://ism.obspm.fr/shock.html>

the large aperture of the LWS in the southern portion of remnant.

Based on the allowed ranges of n_o and v_s , we estimate the ram pressure to be $p_{ram} = \rho v_s^2 \sim n_o v_s^2 \sim 10^{-7}$ dyne cm^{-2} at the bright [O I] and [C II] regions. From X-ray measurements, we can estimate the thermal pressure of the remnant interior, $p_{th} = 2n_e k T_e$, where k is the Boltzmann constant, and n_e and T_e are the postshock electron density and temperature, respectively. Using the n_e and $k T_e$ values reported by Troja et al. (2006), the thermal pressure is $\sim 10^{-9}$ dyne cm^{-2} . The ram pressure is more than two orders of magnitude higher than the thermal pressure, indicating that the shock is radiative. A similarly large difference in the ram and thermal pressure has been observed in other MC-interacting SNRs, W44 and 3C391 (Reach & Rho 1996). Reach & Rho (1996) suggested that the higher ram pressures in regions with bright [O I] and [C II] suggests the presence of dense molecular clumps, while the comparatively low thermal pressures may be from X-ray gas at the interior where the density is relatively low.

RCW 103 – Observations of H₂ emission (Oliva et al. 1989; Burton & Spyromilio 1993) and ¹²CO $J = 1-0$ and HCO⁺ lines (Paron et al. 2006) at the southern shell of RCW 103 indicate an interaction with an MC. The [O I] 63 μm line emission at the southern ridge has been observed with the IRS aboard *Spitzer* (Andersen et al. 2011), and previously with the *ISO* LWS (Oliva et al. 1999), with estimated intensity values of 3.2×10^{-4} and 6.0×10^{-4} ergs $\text{s}^{-1} \text{cm}^{-2} \text{sr}^{-1}$, respectively, roughly equivalent to our estimated value at region # 3 (5.3×10^{-4} ergs $\text{s}^{-1} \text{cm}^{-2} \text{sr}^{-1}$). Based on the strong [O I] 63 μm and 145 μm intensities at the southern ridge, the shock conditions are similar to those in IC 443, and may be the result of either a fast shock – low density or slow shock – high density scenario. However, the level of [C II] 158 μm emission in region # 2 is comparable to region #3, suggesting that most of the [C II] 158 μm flux may originate from background. If the background-subtracted [C II] 158 μm emission is negligible, this is more consistent with the C-shock model with an initial shock speed $v_s \sim 10$ or 30 km s^{-1} , and preshock density $n_o = 10^5 - 10^6 \text{ cm}^{-3}$ (Figure 31c). The background region around RCW 103 is complicated and the ambient [C II] 158 μm emission may vary across the remnant. If the [C II] line flux is truly significantly above the background flux, then there must exist a fast J-type component, similar to the scenario discussed in the case of IC 443. The lower right panel of Figure 15 shows the 2MASS J, H, and K_s band images of RCW 103. Filamentary emission from all three bands is visible at the southern boundary, with the K_s emission located to the

exterior of J and H band emission. Region # 3 more closely coincides with the J and H band emission, suggesting that the region may be dominated more by C-shock conditions – a slower shock traversing into a dense medium. The estimated ram and thermal pressures are roughly equal at the southern ridge ($\sim 10^7$ dyne cm^{-2}), possibly due to dense CSM knots.

Kes 79 – Kes 79 is a several 10^3 yr-old (Zhou et al. 2016; Kuriki et al. 2018) double-shelled SNR, with a central compact object (Giacani et al. 2009). A broad OH absorption feature (Green 1989) and bright HCO⁺ emission have been observed at the east and southeast boundary of Kes 79 near the local standard of rest velocity $V_{LSR} \sim 105 \text{ km s}^{-1}$, consistent with the estimated distance to the SNR of 7.1 kpc based on the Galactic rotation curve (Green & Dewdney 1992). The OH absorption and emission lines are detected both against Kes 79 and the associated pulsar B1849+00 (Stanimirović et al. 2003). The detection of OH lines in Kes 79 suggests an interaction with dense clouds. The detection of nearby CO clouds supports such SNR-cloud interactions (Kilpatrick et al. 2016). Zhou et al. (2016) found a broadened ¹²CO $J = 3-2$ line ($\Delta v = 12 \text{ km s}^{-1}$) along the east, south, and west of the SNR, suggesting MC interactions with the SNR shock. While the broad CO emission coincides with the southern and western radio shell (e.g., around 111 km s^{-1} component), the broad CO emission (e.g., at 103 km s^{-1}) in the east is a few tens of arcseconds to the west of the faint radio shell (Fig. 6d of Zhou et al. 2016). It indicates the interaction is at the front (around 103 km s^{-1}) of Kes 79 in the eastern direction.

The *ISO* pointings are slightly off the peak interacting sites (by up to a few tens of arcseconds) where the broad CO lines are detected. Thus, these *ISO* raster observations may cover only parts of the shock-clouds interacting regions. This is probably why the [O I] 63 μm emission does not show strong enhancement at a particular position but still relatively bright (a factor of 2–3 brighter than those of background emission in IC 443 raster or those of CTB 109). We consider that the *ISO* raster observations may not trace the strongest shock-cloud interacting regions.

CTB 109 – CTB 109 is a $\sim 10^4$ yr-old (Sánchez-Cruces et al. 2018) SNR. It is well-known for its semi-circular shape as seen in radio and X-rays, which has been attributed to the presence of a giant MC at its western boundary (Heydari-Malayeri et al. 1981; Tatematsu et al. 1987; Kothes et al. 2002). However, a search for broad ¹²CO $J = 1-0$ emission, which would indicate interactions between the SNR shock and the cloud, resulted in no detection (Tatematsu et al. 1990). Our

measurements show that the [O I] 63 μm emission is enhanced by a factor of ~ 2 (compared with the background emission to the north) in two regions along the western boundary (3 and 4). The emission is relatively weak, and not clearly indicative of a strong shock interaction (see Figure 30b).

W 28 – W 28 is a few 10^4 yr-old SNR (Velázquez et al. 2002) which exhibits both center-filled X-ray emission and a shell-like structure in radio, and thus belongs to the mixed-morphology class of SNRs (Wootten 1981; Rho & Borkowski 2002; Pannuti et al. 2017). Several molecular lines from H_2O , OH, and CO, and H_2 lines are detected in W 28, and are evidence of a shock passing through molecular gas (Reach & Rho 1998; Arikawa et al. 1999; Reach & Rho 2000). We detect [O I] 63 and 145 μm emission lines which appear which appears consistent with our C-shock model with a high preshock density ($10^4 - 10^6 \text{ cm}^{-3}$) (see Figure 31f). We detect a [C II] 158 μm line that is exceptionally strong, which is consistent with a fast J-shock model (Table 9). The difference in ram and thermal pressures is not as significant in W 28 (a factor of ~ 2) as in IC 443 (a factor of ~ 100). We note that, considering its projected position close to the Galactic plane ($b \sim -0.1^\circ$), the contamination in our measured line flux from the strong Galactic background emission may be significant.

6. CONTINUUM EMISSION IN SNR G320.4-1.2

In the LWS spectra of several SNRs, we clearly detect the continuum emission in the FIR band (40 – 200 μm), originating from cold to warm dust grains. If the observed FIR continuum is associated with the SN ejecta gas, the dust emission spectrum is useful to constrain the dust production in these CC SN explosions. A *Herschel* survey identified FIR emission from SNRs in the Galactic plane, and in a few cases, estimated the dust mass associated with SN ejecta (Chawner et al. 2019, 2020). Here we focus on SNR G320.4-1.2, which was not covered by the *Herschel* survey. The remnant shows a clearly broadened [O III] 88 μm line (Section 4, Figure 29) and a bright continuum (Figure 33). The presence of dust emission associated with high-velocity ejecta and the relatively reliable detector calibrations make this SNR the best candidate to analyze the continuum spectrum in order to constrain the dust mass produced by the SN.

To model the dust emission in this SNR, we fit the continuum spectrum (after the flux normalizations among the individual subdetectors were applied, see Section 2) with a blackbody (BB) model in the form of

$$F_\lambda = \frac{\kappa_\lambda B_\lambda(T) M_{dust}}{D^2}, \quad (1)$$

where F_λ is the flux at each wavelength, λ , κ is the dust mass absorption coefficient, B_λ is the Planck function at temperature T , and M_{dust} and D are the dust mass and distance to the source, respectively. We assumed the distance of $D = 5.2 \text{ kpc}$ for G320.4-1.2 (Gaensler et al. 1999). The dust mass coefficient, κ_λ , is a function of wavelength:

$$\kappa_\lambda = \kappa_{\lambda_0} \left(\frac{\lambda_0}{\lambda} \right)^\beta. \quad (2)$$

We assume that the emission can be described by $\kappa_{\lambda_0} = 0.07 \text{ m}^2 \text{ kg}^{-1}$ for $\lambda_0 = 850 \mu\text{m}$ (James et al. 2002), and $\beta = 1.9$, similar to bulk interstellar dust (Planck Collaboration et al. 2014).

Because our spectrum is not background-subtracted, the observed continuum includes dust emission components from both the SNR and ISM, and thus we apply a two-component BB model. The warm component represents emission associated with the SNR, and the cold component accounts for cold dust in the ISM background emission (Reach et al. 1995; Boulanger et al. 1996; Lagache et al. 1998). Before fitting, we excised the emission lines from the spectrum, leaving only the underlying continuum. We found that, while the observed spectrum is overall well-described by the best-fit model (see Figure 33:Upper), the fit is statistically poor ($\chi_\nu^2 \sim 200$). We realized that the statistical uncertainties on a small fraction of the flux values in the spectrum ($\sim 5\%$ of the total data points) are exceptionally small (typically $\ll 1\%$ of the flux values), which are more than an order of magnitude smaller than the average fractional uncertainties on the rest of the flux values ($\sim 15\%$). This small fraction of data points contributes the total χ_ν^2 almost entirely (by $\sim 98\%$). To mitigate this issue, we manually assign statistical uncertainties on these flux values, adopting the mean uncertainty values for all flux measurements in each subdetector. After this adjustment, the best-fit model significantly improves ($\chi_\nu^2 \sim 4$).

Our best-fit dust temperatures and masses are 46 – 52 K and 0.03 – 0.06 M_\odot for the warm component, and 17 – 20 K and 4 – 15 M_\odot for the cold component. The quoted ranges of these estimates represent the systematic uncertainties due to flux normalizations among subdetectors. The statistical uncertainties are small, on the order of $\lesssim 2\%$. We note that when the SW1 subdetector is used as a baseline, the resulting fit is poorer, and the estimated dust mass is at least 2 times greater than those estimated with other subdetectors as the baseline. Because of this anomaly, we exclude it in our discussion hereafter. The warm component most likely represents the emission spectrum of the SN-created dust, for which

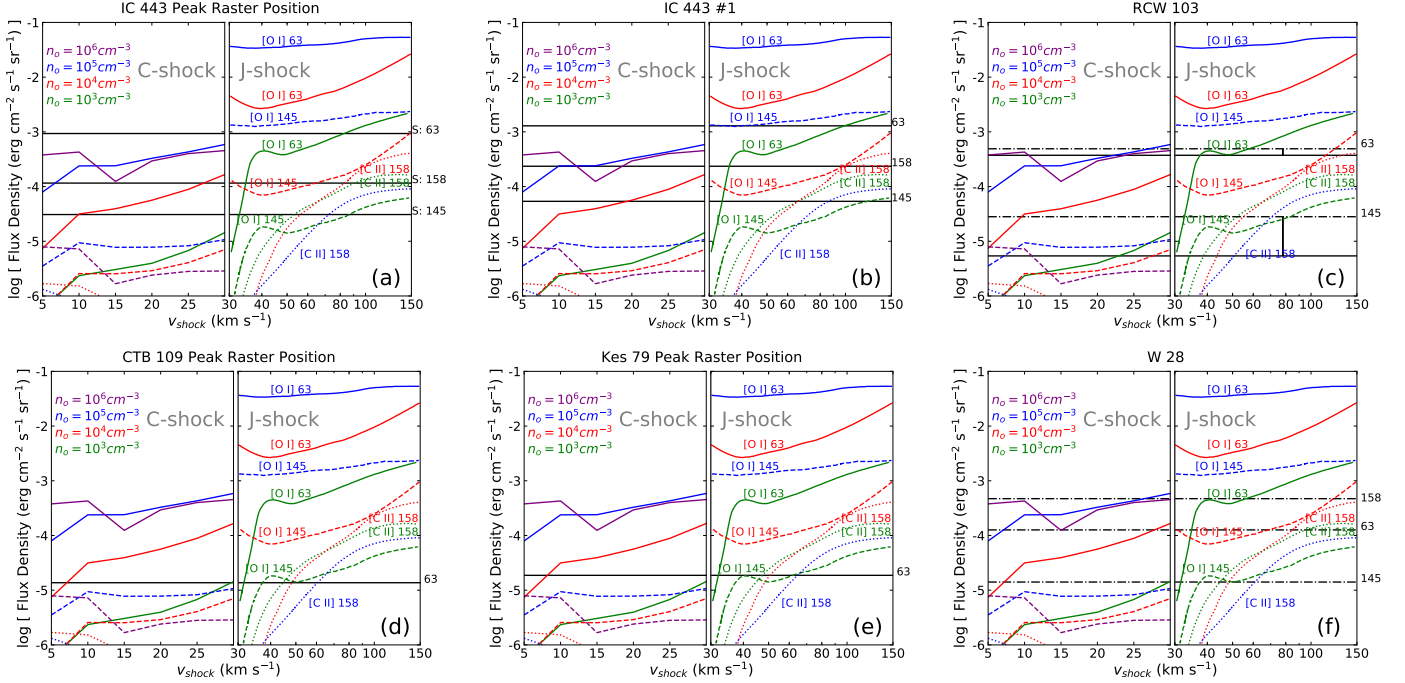


Figure 31. In each panel, the predicted [O I] 63 μm , [O I] 145 μm , [C II] 158 μm line brightness values for a slow C-shock (left side) and fast J-shock (right side) interacting with a molecular cloud. The C-shock line intensities were calculated using the Paris-Durham shock code, while the J-shock intensities are reproduced from Figure 7 of Hollenbach & McKee (1989). The observed background-subtracted line brightness values from *ISO* LWS observations of W 28, IC 443, Kes 79, CTB 109, and RCW 103 are overlaid as solid black horizontal lines. In the W 28 and RCW 103 panels, the total flux density and background-subtracted values are shown as dashed-dotted and solid lines, respectively. The W 28 observation did not include a background measurement.

Table 9. Shock Conditions in SNRs Interacting with Molecular Clouds

SNR	L^* (L_{\odot})	J-shock (n_o, v_s) ($\text{cm}^{-3}, \text{km s}^{-1}$)	C-shock (n_o, v_s) ($\text{cm}^{-3}, \text{km s}^{-1}$)	Pressure (p_{ram}, p_{th}) (dyne cm^{-2})
W 28	2	$10^3, 30 - 40$	$10^4 - 10^6, \sim \mathbf{25}$	$5 \times 10^{-8}, 10^{-9}$
IC 443 #1	10	$10^3, \sim \mathbf{100}$	$10^5 - 10^6, \sim 30$	$10^{-7}, 10^{-9}$
IC 443 #2	5	$10^3, \sim \mathbf{60}$	$10^5 - 10^6, \sim 15$ or ~ 30	—
IC 443 #3	2	$10^3, \mathbf{30 - 40}$	$10^5 - 10^6, 10 - 20$	—
IC 443 Raster (5)	8	$10^3, \sim \mathbf{80}$	$10^5 - 10^6, \sim 10$ or ~ 30	—
RCW 103	15	$10^3, 30 - 50$	$10^5 - 10^6, \sim 10$ or ~ 30	$10^{-7}, 10^{-7}$

*Luminosity values within the *ISO* LWS beam. Thermal pressure calculated using values from Rho & Borkowski (2002), Troja et al. (2006), and Frank et al. (2015) for W 28, IC 443, and RCW 103, respectively. The most favorable model is marked in bold.

we estimate the mass $\sim 0.03 - 0.06 M_{\odot}$. Our best-fit temperature for the cold component is consistent with that for the background ISM dust temperature as measured in literature (Reach et al. 1995; Boulanger et al. 1996; Lagache et al. 1998).

Based on the *ISO* LWS spectrum, G320.4-1.2 is a promising candidate that shows dust emission originating from grains formed in SN ejecta. We clearly detect the [O III] 88 μm with a velocity dispersion of $\sim 2000 \text{ km s}^{-1}$ indicative of high-velocity ejecta. We also

clearly detect a warm (46 – 52 K) dust continuum associated with this SN ejecta feature. The *ISO* beam partially covers the intriguing MIR source, IRAS 15099-5856 (IRAS 15099 hereafter) located at $(\alpha_{2000}, \delta_{2000}) = (15^{\text{h}}13^{\text{m}}56^{\text{s}}32, -59^{\circ}07'40''.9)$ (Koo et al. 2011). IRAS 15099 contains a bright central source, IRS1, surrounded by diffuse fainter emission, with spiral filaments extending out to a few arcminutes (see Figure 32). While the origin of IRAS 15099 is unclear, Arendt (1991) suggested

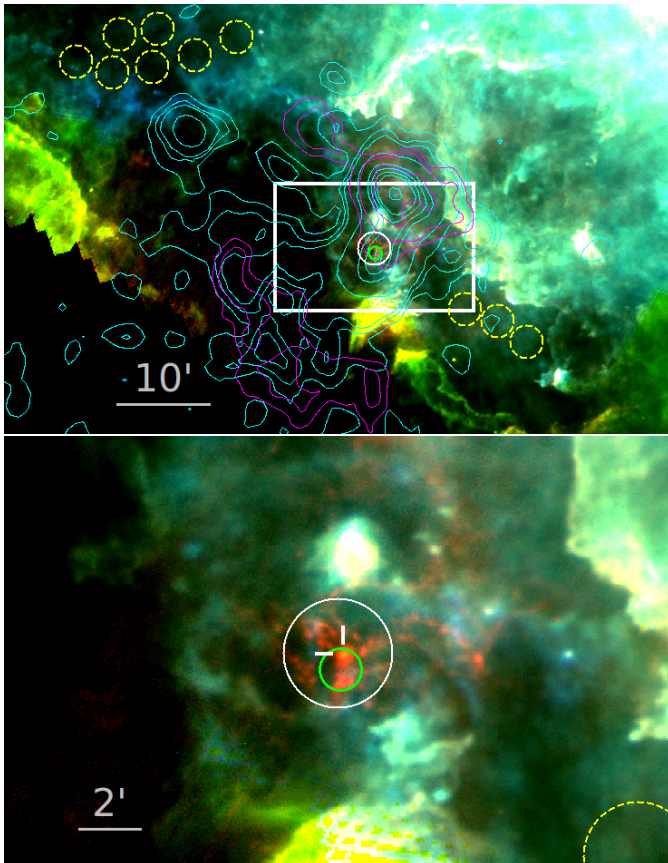


Figure 32. *Herschel* 3-color image (red: 70 μm , green: 160 μm , blue: 250 μm) with the *ISO* LWS beam shown as a green circle (0.67' diameter), while the solid white and dashed-yellow circles (1.7' diameter) shows the *Herschel* photometric target and background regions, respectively. Contours are the same as in Figure 14. Upper: Zoomed-out view showing the overall extent of SNR G320.4–1.2. The white box shows the field of view of the lower panel. Lower: Zoomed-in with contours removed to highlight the bright (in red) filamentary 70 μm emission (from IRAS 15099) near the center of the SNR. The white markers indicate the position of the compact source (IRS1).

that the IR emission may result from dust heated by a hot plasma, or by the nearby O star, Muzzio 10.

Koo et al. (2011) fit the *Spitzer* IRS spectrum of IRS1 with several dust components, and found that most of the emission arises from crystalline olivine and amorphous silicate at $T = 54 - 58$ K. They found a total dust mass of $0.009 \pm 0.001 d_{4\text{kpc}}^2 M_{\odot}$ for IRS1. At a distance of 5.2 kpc, their estimated total dust mass becomes $0.015 M_{\odot}$. We note that, due to the large angular diameter of the beam, it is unclear if the broad [O III] line that we detect is associated with the compact central emission of IRS1, or the surrounding diffuse emission. Thus, our estimated dust mass range is in plausible agreement

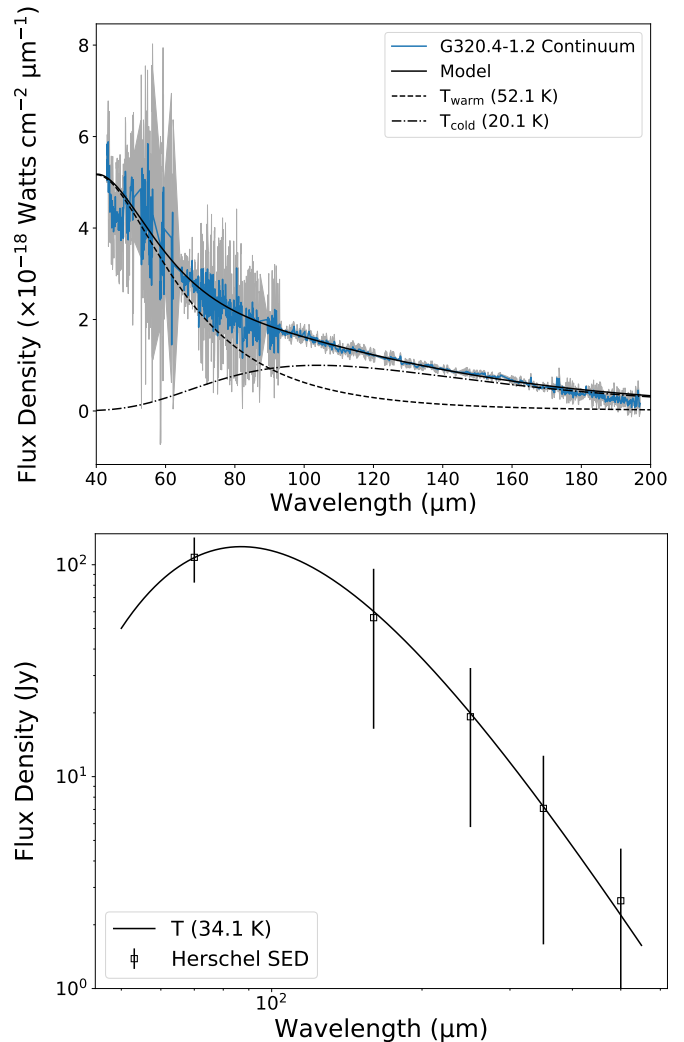


Figure 33. Upper: Continuum spectrum of G320.4–1.2 obtained with the *ISO* LWS, with emission lines removed. Our best-fit two-component blackbody model is overlaid. A warm component ($T \sim 52$ K) dominates the spectrum at $\lambda \lesssim 90$ μm , while the cold component ($T \sim 20$ K) dominates at $\lambda \gtrsim 90$ μm . Lower: *Herschel* background-subtracted SED of the center of G320.4–1.2 fit with our blackbody model, $T \sim 34$ K.

with that by (Koo et al. 2011) roughly within a factor of ~ 2 .

To estimate the background-subtracted dust mass of IRAS 15099, we use the archival *Herschel* PACS (Poglitsch et al. 2010) HPDP images at 70 μm and 160 μm , and SPIRE (Griffin et al. 2010) Level 2.5 images at 250 μm , 350 μm , and 500 μm images of SNR G320.4–1.2 (Observation IDs: 1342203291, 1342203292). Since our *Herschel* extraction aperture diameter (206'') of our regions is larger than the beam size of the maps (FWHM $\leq 35.2''$), we do not apply aperture corrections to the extracted spectral energy distribution (SED).

The emission associated with IRAS 15099 is most clearly visible at 70 μm (see Figure 32). The brightest feature is located at the position of IRS1, with spiral filaments that reach out several arcminutes. Emission associated with IRS1 is clearly detected at 160 μm . Koo et al. (2011) identified emission at 65 μm and 90 μm , but not at 140 μm or 160 μm with the *AKARI* FIS (Far Infrared Surveyor). Thus, we identify clear 160 μm emission from IRS1 for the first time. To measure the net flux from IRAS 15099, we chose a 206'' diameter aperture centered at $(\alpha_{2000}, \delta_{2000}) = (15^{\text{h}}13^{\text{m}}57^{\text{s}}.1980, -59^{\circ}07'39''.78)$ which covers the bulk of the 70 μm emission apparently associated with IRAS 15099. We chose ten background regions to the east and west of the remnant, exterior to the radio and X-ray shell. These regions are covered in the PACS and SPIRE images, and avoid the bright ISM emission to the north (see Figure 32). We estimate net flux densities of 108 ± 26.0 Jy, 56.3 ± 39.4 Jy, 19.2 ± 13.4 Jy, 7.1 ± 5.5 Jy, and 2.6 ± 2.0 Jy at 70 μm , 160 μm , 250 μm , 350 μm , and 500 μm , respectively. The flux from the 206'' diameter aperture increases by about a factor of 3 – 4 over our *ISO*-measured flux. Scaling the aperture sizes between *ISO* and Herschel, we estimate a total dust mass of 0.1 – 0.2 M_{\odot} for our Herschel-measured fluxes.

We fit the *Herschel* background-subtracted SED with a one-component BB model and estimate a total dust mass of $0.66 \pm 0.06 M_{\odot}$ at a temperature of 34 ± 0.6 K. This dust mass is highly dependent on background subtraction, which varies significantly in the region around G320.4–1.2. The discrepancy in the dust mass estimates based on the *Herschel* and *ISO* data may be attributed to these uncertainties. Follow-up observations with higher spatial and spectral resolutions, (e.g., with *JWST* and *SOFIA*), are required to verify if the dust and ejecta emission are clearly correlated. Our estimate for the dust mass associated with ejecta in G320.4–1.2 is in line with the growing number of previously published dust mass estimates in CC SNRs (see Table 8 for values and references).

7. SNR COMPARISON WITH HII REGIONS

We compare the FIR atomic line emission of the SNRs with the HII regions in our sample, W51, NGC 6334, and G159.6–18.5 (Table 3 and Figure 27). In W51 and NGC 6334, we detect a bright continuum and several emission lines, [O III] 52, 88 μm , [N III] 57 μm , [O I] 63, 145 μm , [N II] 122 μm , and [C II] 158 μm . In G159.6–18.5, we detect only the 158 μm [C II] line and weak continuum emission. We note that the [N III] 57 μm line is detected only in the HII regions, and not in the SNRs, although Reach & Rho (2000) found hints of a faint [N

III] 57 μm line flux in W 28, W44, and 3C391 ($< 0.25 \times 10^{-4}$ ergs $\text{s}^{-1} \text{cm}^{-1} \text{sr}^{-1}$). In an *ISO* spectral survey of 45 compact HII regions, Peeters et al. (2002) reported clear [N III] 57 μm detections on $\sim 60\%$ of the sample. The [N III] 57 μm /[N II] 122 μm ratio ranges from $\sim 1 - 10$, suggesting higher ionization states of nitrogen in the HII regions than in the SNRs. The lack of [N III] 57 μm detections in our SNR sample compared with the HII region sample of Peeters et al. (2002) indicates that the presence of strong [N III] 57 μm emission may be a discriminator between SNRs and HII regions.

8. SUMMARY

We have studied the previously unpublished *ISO* LWS spectra of 20 SNRs in the Galaxy and Magellanic Clouds. We detect a number of FIR atomic fine-structure lines, including [O III] at 52 μm and 88 μm , [O I] at 63 μm and 145 μm , [N II] at 122 μm , and [C II] at 158 μm , as well as a bright continuum in several SNRs. We find that

- In several SNRs, we find evidence for broad [O I], [O III], and [N II] lines suggesting emission from high-velocity SN ejecta. We present for the first time a firmly detected broad [O III] 88 μm line in G320.4–1.2, indicative of fast-moving SN ejecta in this SNR. In G21.5–0.9, G29.7–0.3, and the Crab Nebula, we confirm previous detections of broad-line emission and present the lines that were not previously identified as broad in some cases.
- We find marginal evidence of broad lines in G54.1+0.3, RCW 103, E0102.2–7219, N132D, N49, and 0540–69.3. Follow-up high resolution imaging spectroscopy with modern instruments (e.g., *SOFIA* or *JWST*) is required to verify the presence of high velocity ejecta in these SNRs.
- Based on the [O I] emission from IC 443 and RCW 103, we find regions along the southern ridge in both SNRs where the SNR shock is likely interacting with a dense molecular cloud. The strong [C II] 158 μm emission in IC 443 indicates the presence of fast J-type shocks.
- We apply a two-component blackbody model fit to the LWS continuum of G320.4–1.2, and estimate a dust mass $\sim 0.1 - 0.2 M_{\odot}$ and temperature of ~ 50 K associated with SN ejecta.
- We detect the [N III] 57 μm line only in our HII region sample. This distinctive spectral characteristic may serve as a discriminator in the identification of HII regions and SNRs.

The version of the *ISO* data presented in this paper correspond to the Highly Processed Data Product (HPDP) set called “Uniformly processed LWS L01 spectra” by C. Lloyd, M. Lerate and T. Grundy, available for public use in the *ISO* Data Archive <http://nida.esac.esa.int/nida-cl-web/>. The authors thank L.N. Tram, B. Godard, and A. Gusdorf for their helpful advice on running the Paris–Durham shock code. We also thank A.

Herbst for compiling the initial dataset. We thank P. Zhou for providing the CO map of Kes 79. We thank G. Sloan, K. Kraemer, and W. Reach for discussions on *ISO* data and IR emission from supernova remnants. This work was in part supported by NASA 2ADAP grant 80NSSC20K0449.

APPENDIX

A. ARCHIVAL LWS SNR DATA NOT INCLUDED IN THIS WORK

In Table A.1 we list the SNRs observed with the *ISO* LWS that were not included in our sample. In most cases, we did not choose these data because they were previously published. In other cases, the data quality was poor and suffered from inadequate sampling of emission line profiles.

Table A.1. *ISO* LWS SNR Observations Not in Our Sample

Name	Target Name*	RA, DEC (J2000)	Date	t_{on} (s)	Publications
G6.4–0.1	W28masA	18 ^h 01 ^m 52 ^s .32 –23°19′25″.7	1997-03-17	1346	1,2,12
G10.0–00.3	SGR1806-20	18 ^h 08 ^m 40 ^s .30 –20°24′40″.9	1997-03-23	730	–
G10.0–00.3	SGR1806-20 Bkg	18 ^h 08 ^m 23 ^s .72 –20°29′42″.1	1997-03-23	729	–
G31.9+0.0	3C391	18 ^h 49 ^m 20 ^s .95 –00°55′48″.4	1996-04-28	1414	1,2,10,12
G31.9+0.0	3C391mol	18 ^h 49 ^m 21 ^s .93 –00°57′22″.1	1997-03-10	1300	1,2,12
G31.9+0.0	3C391mol (L04)	18 ^h 49 ^m 21 ^s .93 –00°57′22″.1	1997-03-10	962	2,12
G31.9+0.0	3C391H20 (L02)	18 ^h 49 ^m 21 ^s .95 –00°57′22″.9	1997-10-26	1720	1,2,12
G31.9+0.0	3C391cut2 (L02)	18 ^h 49 ^m 26 ^s .80 –00°55′48″.7	1997-03-10	892	1,2,12
G31.9+0.0	3C391cut3 (L02)	18 ^h 49 ^m 31 ^s .79 –00°55′20″.4	1997-03-10	824	1,2,12
G31.9+0.0	3C391cut4 (L02)	18 ^h 49 ^m 17 ^s .32 –00°57′04″.4	1997-03-10	754	1,2,12
G34.7–0.4	W44 (L02) 1	18 ^h 56 ^m 32 ^s .41 +01°28′15″.6	1996-04-28	1680	1,2,10,11,12
G34.7–0.4	W44 (L02) 2	18 ^h 56 ^m 28 ^s .37 +01°29′59″.3	1996-04-28	1462	1,2,10,11,12
G34.7–0.4	W44cut3 (L02)	18 ^h 56 ^m 00 ^s .36 +01°12′49″.00	1997-03-10	1520	2,12
G34.7–0.4	W44masA	18 ^h 56 ^m 28 ^s .33s +01°29′58″.90	1997-03-10	962	2,12
G34.7–0.4	W44masA (L04)	18 ^h 56 ^m 28 ^s .33 +01°29′59″.00	1997-03-10	1300	2,12
G35.2–1.7	W48 (L04)	19 ^h 01 ^m 47 ^s .60 +01°13′6″.10	1996-10-24	2312	–
G042.8+00.6	SGR1900+14	19 ^h 07 ^m 15 ^s .22 +09°19′21″.6	1996-09-27	978	–
G042.8+00.6	SGR1900+14 (Bkg)	19 ^h 07 ^m 09 ^s .18 +09°15′21″.3	1997-03-29	1029	–
G111.7–2.1	Cas A #1	23 ^h 23 ^m 27 ^s .75 +58°48′47″.0	1996-06-24	1054	13
G111.7–2.1	Cas A #2	23 ^h 23 ^m 26 ^s .74 +58°50′09″.9	1996-06-24	1052	13
G111.7–2.1	Cas A #3	23 ^h 23 ^m 18 ^s .70 +58°47′30″.8	1996-06-24	1054	13
G111.7–2.1	Cas A #4	23 ^h 23 ^m 53 ^s .94 +58°50′24″.3′	1996-06-24	1054	13
G111.7–2.1	Cas A #5	23 ^h 23 ^m 38 ^s .33 +58°49′22″.1	1997-06-09	1612	13
G111.7–2.1	Cas A #6	23 ^h 23 ^m 35 ^s .12 +58°47′38″.0	1997-06-09	1612	13
G111.7–2.1	Cas A #7	23 ^h 23 ^m 16 ^s .47 +58°49′07″.8	1997-06-02	1614	13

Table A.1 continued

Table A.1 (*continued*)

Name	Target Name*	RA, DEC (J2000)	Date	t_{on} (s)	Publications
G184.6–05.8	Crab Nebula #1	05 ^h 34 ^m 34 ^s .27 +22°01′02″.4	1997-10-11	1124	14,17
G184.6–05.8	Crab Nebula #2	05 ^h 34 ^m 31 ^s .94 +22°02′04″.8	1997-10-09	1126	14,17
G184.6–05.8	Crab Nebula #3	05 ^h 34 ^m 29 ^s .31 +22°00′37″.0	1997-10-09	1124	14,17
G184.6–05.8	Crab Nebula #4	05 ^h 34 ^m 34 ^s .19 +21°59′54″.7	1997-10-09	1630	14,17
G184.6–05.8	Crab Nebula (L02 Narrow)	05 ^h 34 ^m 32 ^s .02 +22°02′04″.5	1998-02-19	1184	–
G184.6–05.8	Crab Nebula (L02 Narrow)	05 ^h 34 ^m 32 ^s .02 +22°02′04″.6	1998-04-04	1184	–
G189.1+3.0	IC443cut	06 ^h 17 ^m 49 ^s .69 +22°45′28″.4	1998-03-13	1218	3, 12
G189.1+3.0	IC443 – C FP Scan (L04) 1.	06 ^h 17 ^m 42 ^s .80 +22°21′37″.7	1998-03-13	1574	–
G189.1+3.0	IC443 – C FP Scan (L04) 2.	06 ^h 17 ^m 07 ^s .64 +22°25′34″.7	1998-04-04	2230	–
G315.4–2.3	RCW 86	14 ^h 43 ^m 04 ^s .20 –62°27′44″.4	1996-02-14	812	–
G332.4–0.4	RCW103 H2+ion	16 ^h 17 ^m 35 ^s .78 –51°06′18″.6	1996-02-23	4160	4,5
J0047.2–7308	SMC0045 (L04)	00 ^h 47 ^m 17 ^s .06 –73°08′29″.3	1997-05-11	1694	–
J0048.5–7319	SMC0046 0 (L04)	00 ^h 48 ^m 25 ^s .43 –73°19′16″.3	1997-05-11	1020	–
J0059.4–7210	SMC N66	00 ^h 59 ^m 08 ^s .02 –72°10′25″.97	1996-04-01	815	6,8,9
J0535–6916	SN 1987A	05 ^h 35 ^m 28 ^s .04 –69°16′11″.7	1998-02-04	3428	15,16
J0537.8–6910	LMC-N157B	05 ^h 37 ^m 51 ^s .76 –69°10′22″.0	1996-04-29	1054	8,9

NOTE—1. (Reach & Rho 1998) 2. (Reach & Rho 2000) 3. (Rho et al. 2001) 4. (Oliva et al. 1998) 5. (Oliva et al. 1999) 6. (Liseau et al. 2006) 7. (He et al. 2005) 8. (Vermeij & van der Hulst 2002) 9. (Vermeij et al. 2002) 10. (Reach & Rho 1996) 11. (Cox et al. 1999) 12. (Yuan & Neufeld 2011) 13. (Docenko & Sunyaev 2010) 14. (Green et al. 2004) 15. (Lundqvist et al. 1999) 16. (Sollerman 2002) 17. (Gomez et al. 2012)

*The observing mode is in parentheses. L01–L02: Grating, L03–L04: Fabry–Pérot.

B. PARIS–DURHAM MODELS

The line intensities of the C–shock models presented in Figure 31 are computed using the Paris–Durham shock code, which simulates the progression of a shock wave through a gaseous medium (Godard et al. 2019). By incorporating relevant heating, cooling, and grain processes, as well as a network of chemical reactions, the code finds the kinematic, thermodynamic, and chemical properties of the shocked layer. These models assume that the shock is irradiated by an external radiation field. Thus, the model contains a pre-shock radiative buffer created by the coupling of the radiation field with the inferred molecular cloud.

To account for an irradiated shock, we run the code in three stages. In the first stage, the code calculates the chemical and thermal conditions at the border of the radiative buffer and the diffuse interstellar medium. In the second stage, the conditions inside the buffer are evolved until the desired extinction (A_v) value is reached. Here, we choose the standard A_v value of 10^{-1} (Godard et al. 2019). In the final stage, the propagation of the shock is computed. In this stage, we performed multiple runs to calculate the model line fluxes for a range of shock velocities ($v_s = 5 - 30 \text{ km s}^{-1}$) and pre-shock densities

($n_o = 10^3 - 10^6 \text{ cm}^{-3}$). We compared the resulting [O I] 63 and 145 μm and [C II] 158 μm line intensities for each model with our measured values (see Figure 31). The relevant input parameters are listed in Table B.1.

Table B.1. Paris–Durham Input Parameters

Parameter	Value
n_H , pre-shock proton density	$10^3 - 10^6 \text{ cm}^{-3}$
G_o , radiation field scaling factor	1
A_V^o , pre-shock visual extinction	0.1
V_s , shock speed	$5 - 30 \text{ km s}^{-1}$
b , magnetic field parameter	1 ^a
ζ_{H_2} , H ₂ cosmic ray ionization rate	$3 \times 10^{-17} \text{ s}^{-1}$
u_{turb} , turbulent velocity	1 km s^{-1}
$timeJ$, shock age	$10^3 - 10^4 \text{ yr}$

^aDimensionless value of the initial magnetic field transverse to the plane of the shock, $b = B_o[\mu G]/(n_H)^{1/2}$.

REFERENCES

- Alan, N., Park, S., & Bilir, S. 2019, *ApJ*, 873, 53, doi: [10.3847/1538-4357/aaf882](https://doi.org/10.3847/1538-4357/aaf882)
- Andersen, M., Rho, J., Reach, W. T., Hewitt, J. W., & Bernard, J. P. 2011, *ApJ*, 742, 7, doi: [10.1088/0004-637X/742/1/7](https://doi.org/10.1088/0004-637X/742/1/7)
- Arendt, R. G. 1991, *AJ*, 101, 2160, doi: [10.1086/115838](https://doi.org/10.1086/115838)
- Arikawa, Y., Tatematsu, K., Sekimoto, Y., & Takahashi, T. 1999, *PASJ*, 51, L7
- Bennett, C. L., Fixsen, D. J., Hinshaw, G., et al. 1994, *ApJ*, 434, 587, doi: [10.1086/174761](https://doi.org/10.1086/174761)
- Bertoldi, F., Carilli, C. L., Cox, P., et al. 2003, *A&A*, 406, L55, doi: [10.1051/0004-6361/20030710](https://doi.org/10.1051/0004-6361/20030710)
- Bietenholz, M. F., & Bartel, N. 2008, *MNRAS*, 386, 1411, doi: [10.1111/j.1365-2966.2008.13058.x](https://doi.org/10.1111/j.1365-2966.2008.13058.x)
- Bilikova, J., Williams, R. N. M., Chu, Y. H., Gruendl, R. A., & Lundgren, B. F. 2007, *AJ*, 134, 2308, doi: [10.1086/522302](https://doi.org/10.1086/522302)
- Blair, W. P., Sankrit, R., Shelton, R., et al. 2000, *ApJL*, 538, L61, doi: [10.1086/312793](https://doi.org/10.1086/312793)
- Bocchino, F., Bandiera, R., & Gelfand, J. 2010, *A&A*, 520, A71, doi: [10.1051/0004-6361/201014298](https://doi.org/10.1051/0004-6361/201014298)
- Borkowski, K. J., Reynolds, S. P., & Miltich, W. 2020, *ApJL*, 895, L32, doi: [10.3847/2041-8213/ab91c0](https://doi.org/10.3847/2041-8213/ab91c0)
- Boulanger, F., Abergel, A., Bernard, J. P., et al. 1996, *A&A*, 312, 256
- Burton, M., & Spyromilio, J. 1993, *Proceedings of the Astronomical Society of Australia*, 10, 327
- Burton, M. G., Geballe, T. R., Brand, P. W. J. L., & Webster, A. S. 1988, *MNRAS*, 231, 617, doi: [10.1093/mnras/231.3.617](https://doi.org/10.1093/mnras/231.3.617)
- Burton, M. G., Hollenbach, D. J., & Tielens, A. G. G. M. 1990, *ApJ*, 365, 620, doi: [10.1086/169516](https://doi.org/10.1086/169516)
- Carter, L. M., Dickel, J. R., & Bomans, D. J. 1997, *PASP*, 109, 990, doi: [10.1086/133971](https://doi.org/10.1086/133971)
- Cesarsky, C. J., & Salama, A. 2006, *ISO Science Legacy*, Vol. 119
- Cesarsky, D., Cox, P., Pineau des Forêts, G., et al. 1999, *A&A*, 348, 945. <https://arxiv.org/abs/astro-ph/9906380>
- Cha, H., Rho, J., An, H., & Millard, M. 2021, submitted to *ApJ*
- Chawner, H., Marsh, K., Matsuura, M., et al. 2019, *MNRAS*, 483, 70, doi: [10.1093/mnras/sty2942](https://doi.org/10.1093/mnras/sty2942)
- Chawner, H., Gomez, H. L., Matsuura, M., et al. 2020, *MNRAS*, 493, 2706, doi: [10.1093/mnras/staa221](https://doi.org/10.1093/mnras/staa221)
- Clegg, P. E., Ade, P. A. R., Armand, C., et al. 1996, *A&A*, 315, L38
- Cox, D. P., Shelton, R. L., Maciejewski, W., et al. 1999, *ApJ*, 524, 179, doi: [10.1086/307781](https://doi.org/10.1086/307781)
- De Looze, I., Barlow, M. J., Bandiera, R., et al. 2019, *MNRAS*, 488, 164, doi: [10.1093/mnras/stz1533](https://doi.org/10.1093/mnras/stz1533)
- Denoyer, L. K. 1979, *ApJL*, 232, L165, doi: [10.1086/183057](https://doi.org/10.1086/183057)
- Dickman, R. L., Snell, R. L., Ziurys, L. M., & Huang, Y.-L. 1992, *ApJ*, 400, 203, doi: [10.1086/171987](https://doi.org/10.1086/171987)
- Docenko, D., & Sunyaev, R. A. 2010, *A&A*, 509, A59, doi: [10.1051/0004-6361/200810366](https://doi.org/10.1051/0004-6361/200810366)
- Dwek, E., & Arendt, R. G. 2008, *ApJ*, 685, 976, doi: [10.1086/589988](https://doi.org/10.1086/589988)
- Finkelstein, S. L., Morse, J. A., Green, J. C., et al. 2006, *ApJ*, 641, 919, doi: [10.1086/500570](https://doi.org/10.1086/500570)
- Flanagan, K. A., Canizares, C. R., Dewey, D., et al. 2004, *ApJ*, 605, 230, doi: [10.1086/382145](https://doi.org/10.1086/382145)
- Frank, K. A., Burrows, D. N., & Park, S. 2015, *ApJ*, 810, 113, doi: [10.1088/0004-637X/810/2/113](https://doi.org/10.1088/0004-637X/810/2/113)
- Gaensler, B. M., Brazier, K. T. S., Manchester, R. N., Johnston, S., & Green, A. J. 1999, *MNRAS*, 305, 724, doi: [10.1046/j.1365-8711.1999.02500.x](https://doi.org/10.1046/j.1365-8711.1999.02500.x)
- Gelfand, J. D., Slane, P. O., & Temim, T. 2015, *ApJ*, 807, 30, doi: [10.1088/0004-637X/807/1/30](https://doi.org/10.1088/0004-637X/807/1/30)
- Giacani, E., Smith, M. J. S., Dubner, G., et al. 2009, *A&A*, 507, 841, doi: [10.1051/0004-6361/200912253](https://doi.org/10.1051/0004-6361/200912253)
- Godard, B., Pineau des Forêts, G., Lesaffre, P., et al. 2019, *A&A*, 622, A100, doi: [10.1051/0004-6361/201834248](https://doi.org/10.1051/0004-6361/201834248)
- Gomez, H. L., Krause, O., Barlow, M. J., et al. 2012, *ApJ*, 760, 96, doi: [10.1088/0004-637X/760/1/96](https://doi.org/10.1088/0004-637X/760/1/96)
- Gotthelf, E. V., Vasisht, G., Boylan-Kolchin, M., & Torii, K. 2000, *ApJL*, 542, L37, doi: [10.1086/312923](https://doi.org/10.1086/312923)
- Green, D. A. 1989, *MNRAS*, 238, 737, doi: [10.1093/mnras/238.3.737](https://doi.org/10.1093/mnras/238.3.737)
- Green, D. A., & Dewdney, P. E. 1992, *MNRAS*, 254, 686, doi: [10.1093/mnras/254.4.686](https://doi.org/10.1093/mnras/254.4.686)
- Green, D. A., Tuffs, R. J., & Popescu, C. C. 2004, *MNRAS*, 355, 1315, doi: [10.1111/j.1365-2966.2004.08414.x](https://doi.org/10.1111/j.1365-2966.2004.08414.x)
- Griffin, M. J., Abergel, A., Abreu, A., et al. 2010, *A&A*, 518, L3, doi: [10.1051/0004-6361/201014519](https://doi.org/10.1051/0004-6361/201014519)
- Gry, C., Swinyard, B., Harwood, A., et al. 2003, *The ISO Handbook, Volume III - LWS - The Long Wavelength Spectrometer*
- Guest, B. T., Safi-Harb, S., & Tang, X. 2019, *MNRAS*, 482, 1031, doi: [10.1093/mnras/sty2635](https://doi.org/10.1093/mnras/sty2635)
- Hattori, S., Straal, S. M., Zhang, E., et al. 2020, *ApJ*, 904, 32, doi: [10.3847/1538-4357/abba32](https://doi.org/10.3847/1538-4357/abba32)
- He, J. H., Szczerba, R., Chen, P. S., & Sobolev, A. M. 2005, *A&A*, 434, 201, doi: [10.1051/0004-6361:20040569](https://doi.org/10.1051/0004-6361:20040569)
- Heydari-Malayeri, M., Kahane, C., & Lucas, R. 1981, *Nature*, 293, 549, doi: [10.1038/293549a0](https://doi.org/10.1038/293549a0)
- Hirashita, H., Burgarella, D., & Bouwens, R. J. 2017, *MNRAS*, 472, 4587, doi: [10.1093/mnras/stx2349](https://doi.org/10.1093/mnras/stx2349)

- Hollenbach, D., & McKee, C. F. 1989, *ApJ*, 342, 306, doi: [10.1086/167595](https://doi.org/10.1086/167595)
- Isaak, K. G., Priddey, R. S., McMahan, R. G., et al. 2002, *MNRAS*, 329, 149, doi: [10.1046/j.1365-8711.2002.04966.x](https://doi.org/10.1046/j.1365-8711.2002.04966.x)
- James, A., Dunne, L., Eales, S., & Edmunds, M. G. 2002, *MNRAS*, 335, 753, doi: [10.1046/j.1365-8711.2002.05660.x](https://doi.org/10.1046/j.1365-8711.2002.05660.x)
- Kessler, M. F., Steinz, J. A., Anderegg, M. E., et al. 1996, *A&A*, 500, 493
- Kilpatrick, C. D., Biegging, J. H., & Rieke, G. H. 2016, *ApJ*, 816, 1, doi: [10.3847/0004-637X/816/1/1](https://doi.org/10.3847/0004-637X/816/1/1)
- Kirshner, R. P., Morse, J. A., Winkler, P. F., & Blair, W. P. 1989, *ApJ*, 342, 260, doi: [10.1086/167590](https://doi.org/10.1086/167590)
- Kokusho, T., Torii, H., Nagayama, T., et al. 2020, *ApJ*, 899, 49, doi: [10.3847/1538-4357/ab9cb3](https://doi.org/10.3847/1538-4357/ab9cb3)
- Koo, B.-C., McKee, C. F., Suh, K.-W., et al. 2011, *ApJ*, 732, 6, doi: [10.1088/0004-637X/732/1/6](https://doi.org/10.1088/0004-637X/732/1/6)
- Kothes, R., Uyaniker, B., & Yar, A. 2002, *ApJ*, 576, 169, doi: [10.1086/341545](https://doi.org/10.1086/341545)
- Kuriki, M., Sano, H., Kuno, N., et al. 2018, *ApJ*, 864, 161, doi: [10.3847/1538-4357/aad7be](https://doi.org/10.3847/1538-4357/aad7be)
- Lagache, G., Abergel, A., Boulanger, F., & Puget, J. L. 1998, *A&A*, 333, 709. <https://arxiv.org/abs/astro-ph/9812474>
- Laporte, N., Ellis, R. S., Boone, F., et al. 2017, *ApJL*, 837, L21, doi: [10.3847/2041-8213/aa62aa](https://doi.org/10.3847/2041-8213/aa62aa)
- Law, C. J., Milisavljevic, D., Patnaude, D. J., et al. 2020, *ApJ*, 894, 73, doi: [10.3847/1538-4357/ab873a](https://doi.org/10.3847/1538-4357/ab873a)
- Leahy, D. A., Tian, W., & Wang, Q. D. 2008, *AJ*, 136, 1477, doi: [10.1088/0004-6256/136/4/1477](https://doi.org/10.1088/0004-6256/136/4/1477)
- Leahy, D. A., & Tian, W. W. 2008, *A&A*, 480, L25, doi: [10.1051/0004-6361:20079149](https://doi.org/10.1051/0004-6361:20079149)
- Leisawitz, D., Amatucci, E., Allen, L., et al. 2021, *Journal of Astronomical Telescopes, Instruments, and Systems*, 7, 011014, doi: [10.1117/1.JATIS.7.1.011014](https://doi.org/10.1117/1.JATIS.7.1.011014)
- Liseau, R., Justtanont, K., & Tielens, A. G. G. M. 2006, *A&A*, 446, 561, doi: [10.1051/0004-6361:20053925](https://doi.org/10.1051/0004-6361:20053925)
- Liu, X. W., Barlow, M. J., Cohen, M., et al. 2001, *MNRAS*, 323, 343, doi: [10.1046/j.1365-8711.2001.04180.x](https://doi.org/10.1046/j.1365-8711.2001.04180.x)
- Lloyd, C., Lerate, M. R., & Grundy, T. R. 2003, *The LWS L01 Pipeline*. http://ida.esac.esa.int/8080/hdpdp/technical_reports/technote34.html
- Lundqvist, N., Lundqvist, P., Björnsson, C. I., et al. 2011, *MNRAS*, 413, 611, doi: [10.1111/j.1365-2966.2010.18159.x](https://doi.org/10.1111/j.1365-2966.2010.18159.x)
- Lundqvist, P., Sollerman, J., Kozma, C., et al. 1999, *A&A*, 347, 500. <https://arxiv.org/abs/astro-ph/9905389>
- Lundqvist, P., Lundqvist, N., Vlahakis, C., et al. 2020, *MNRAS*, 496, 1834, doi: [10.1093/mnras/staa1675](https://doi.org/10.1093/mnras/staa1675)
- Mathewson, D. S., Dopita, M. A., Tuohy, I. R., & Ford, V. L. 1980, *ApJL*, 242, L73, doi: [10.1086/183406](https://doi.org/10.1086/183406)
- Morgan, H. L., & Edmunds, M. G. 2003, *MNRAS*, 343, 427, doi: [10.1046/j.1365-8711.2003.06681.x](https://doi.org/10.1046/j.1365-8711.2003.06681.x)
- Morse, J. A., Winkler, P. F., & Kirshner, R. P. 1995, *AJ*, 109, 2104, doi: [10.1086/117436](https://doi.org/10.1086/117436)
- Nakagawa, T., Yui, Y. Y., Doi, Y., et al. 1998, *ApJS*, 115, 259, doi: [10.1086/313082](https://doi.org/10.1086/313082)
- Newville, M., Stensitzki, T., Allen, D. B., & Ingargiola, A. 2014, *LMFIT: Non-Linear Least-Square Minimization and Curve-Fitting for Python, 0.8.0*, Zenodo, doi: [10.5281/zenodo.11813](https://doi.org/10.5281/zenodo.11813)
- Nozawa, T., Kozasa, T., Umeda, H., Maeda, K., & Nomoto, K. 2003, *ApJ*, 598, 785, doi: [10.1086/379011](https://doi.org/10.1086/379011)
- Oliva, E., Drapatz, S., Lutz, D., Sturm, E., & Moorwood, A. F. M. 1998, *Ap&SS*, 255, 211, doi: [10.1023/A:1001146631433](https://doi.org/10.1023/A:1001146631433)
- Oliva, E., Moorwood, A. F. M., & Danziger, I. J. 1989, *A&A*, 214, 307
- Oliva, E., Moorwood, A. F. M., Drapatz, S., Lutz, D., & Sturm, E. 1999, *A&A*, 343, 943
- Otsuka, M., van Loon, J. T., Long, K. S., et al. 2010, *A&A*, 518, L139, doi: [10.1051/0004-6361/201014642](https://doi.org/10.1051/0004-6361/201014642)
- Owen, P. J., & Barlow, M. J. 2015, *ApJ*, 801, 141, doi: [10.1088/0004-637X/801/2/141](https://doi.org/10.1088/0004-637X/801/2/141)
- Pannuti, T. G., Rho, J., Kargaltsev, O., et al. 2017, *ApJ*, 839, 59, doi: [10.3847/1538-4357/aa615c](https://doi.org/10.3847/1538-4357/aa615c)
- Park, S., Burrows, D. N., Garmire, G. P., et al. 2003, *ApJ*, 586, 210, doi: [10.1086/367619](https://doi.org/10.1086/367619)
- Park, S., Hughes, J. P., Slane, P. O., et al. 2012, *ApJ*, 748, 117, doi: [10.1088/0004-637X/748/2/117](https://doi.org/10.1088/0004-637X/748/2/117)
- Park, S., Hughes, J. P., Slane, P. O., Mori, K., & Burrows, D. N. 2010, *ApJ*, 710, 948, doi: [10.1088/0004-637X/710/2/948](https://doi.org/10.1088/0004-637X/710/2/948)
- Paron, S. A., Reynoso, E. M., Purcell, C., Dubner, G. M., & Green, A. 2006, *PASA*, 23, 69, doi: [10.1071/AS06003](https://doi.org/10.1071/AS06003)
- Peeters, E., Martín-Hernández, N. L., Damour, F., et al. 2002, *A&A*, 381, 571, doi: [10.1051/0004-6361:20011516](https://doi.org/10.1051/0004-6361:20011516)
- Pineda, J. L., Langer, W. D., Velusamy, T., & Goldsmith, P. F. 2013, *A&A*, 554, A103, doi: [10.1051/0004-6361/201321188](https://doi.org/10.1051/0004-6361/201321188)
- Pinheiro Gonçalves, D., Noriega-Crespo, A., Paladini, R., Martin, P. G., & Carey, S. J. 2011, *AJ*, 142, 47, doi: [10.1088/0004-6256/142/2/47](https://doi.org/10.1088/0004-6256/142/2/47)
- Planck Collaboration, Ade, P. A. R., Aghanim, N., et al. 2014, *A&A*, 564, A45, doi: [10.1051/0004-6361/201322367](https://doi.org/10.1051/0004-6361/201322367)
- Poglitsch, A., Waelkens, C., Geis, N., et al. 2010, *A&A*, 518, L2, doi: [10.1051/0004-6361/201014535](https://doi.org/10.1051/0004-6361/201014535)
- Reach, W. T., & Rho, J. 1996, *A&A*, 315, L277
- . 1998, *ApJL*, 507, L93, doi: [10.1086/311672](https://doi.org/10.1086/311672)
- . 2000, *ApJ*, 544, 843, doi: [10.1086/317252](https://doi.org/10.1086/317252)

- Reach, W. T., Tram, L. N., Richter, M., Gusdorf, A., & DeWitt, C. 2019, *ApJ*, 884, 81, doi: [10.3847/1538-4357/ab41f7](https://doi.org/10.3847/1538-4357/ab41f7)
- Reach, W. T., Dwek, E., Fixsen, D. J., et al. 1995, *ApJ*, 451, 188, doi: [10.1086/176210](https://doi.org/10.1086/176210)
- Reynolds, S. P. 1985, *ApJ*, 291, 152, doi: [10.1086/163050](https://doi.org/10.1086/163050)
- Reynoso, E. M., Green, A. J., Johnston, S., et al. 2004, *PASA*, 21, 82, doi: [10.1071/AS03053](https://doi.org/10.1071/AS03053)
- Rho, J., & Borkowski, K. J. 2002, *ApJ*, 575, 201, doi: [10.1086/341192](https://doi.org/10.1086/341192)
- Rho, J., Jarrett, T. H., Cutri, R. M., & Reach, W. T. 2001, *ApJ*, 547, 885, doi: [10.1086/318398](https://doi.org/10.1086/318398)
- Rho, J., & Petre, R. 1997, *ApJ*, 484, 828, doi: [10.1086/304350](https://doi.org/10.1086/304350)
- Rho, J., Reach, W. T., Tappe, A., et al. 2009, *ApJ*, 700, 579, doi: [10.1088/0004-637X/700/1/579](https://doi.org/10.1088/0004-637X/700/1/579)
- Rho, J., Gomez, H. L., Boogert, A., et al. 2018, *MNRAS*, 479, 5101, doi: [10.1093/mnras/sty1713](https://doi.org/10.1093/mnras/sty1713)
- Sánchez-Cruces, M., Rosado, M., Fuentes-Carrera, I., & Ambrocio-Cruz, P. 2018, *MNRAS*, 473, 1705, doi: [10.1093/mnras/stx2460](https://doi.org/10.1093/mnras/stx2460)
- Sarangi, A., & Cherneteff, I. 2015, *A&A*, 575, A95, doi: [10.1051/0004-6361/201424969](https://doi.org/10.1051/0004-6361/201424969)
- Seitenzahl, I. R., Vogt, F. P. A., Terry, J. P., et al. 2018, *ApJL*, 853, L32, doi: [10.3847/2041-8213/aaa958](https://doi.org/10.3847/2041-8213/aaa958)
- Seok, J. Y., Koo, B.-C., Onaka, T., et al. 2008, *PASJ*, 60, S453, doi: [10.1093/pasj/60.sp2.S453](https://doi.org/10.1093/pasj/60.sp2.S453)
- Sharda, P., Gaetz, T. J., Kashyap, V. L., & Plucinsky, P. P. 2020, *ApJ*, 894, 145, doi: [10.3847/1538-4357/ab8a46](https://doi.org/10.3847/1538-4357/ab8a46)
- Sluder, A., Milosavljević, M., & Montgomery, M. H. 2018, *MNRAS*, 480, 5580, doi: [10.1093/mnras/sty2060](https://doi.org/10.1093/mnras/sty2060)
- Smith, N. 2013, *MNRAS*, 434, 102, doi: [10.1093/mnras/stt1004](https://doi.org/10.1093/mnras/stt1004)
- Snell, R. L., Hollenbach, D., Howe, J. E., et al. 2005, *ApJ*, 620, 758, doi: [10.1086/427231](https://doi.org/10.1086/427231)
- Sollerman, J. 2002, *NewAR*, 46, 493, doi: [10.1016/S1387-6473\(02\)00189-6](https://doi.org/10.1016/S1387-6473(02)00189-6)
- Stanimirović, S., Weisberg, J. M., Dickey, J. M., et al. 2003, *ApJ*, 592, 953, doi: [10.1086/375779](https://doi.org/10.1086/375779)
- Su, Y., Chen, Y., Yang, J., et al. 2009, *The Astrophysical Journal*, 694, 376, doi: [10.1088/0004-637x/694/1/376](https://doi.org/10.1088/0004-637x/694/1/376)
- Tappe, A., Rho, J., Boersma, C., & Micelotta, E. R. 2012, *ApJ*, 754, 132, doi: [10.1088/0004-637X/754/2/132](https://doi.org/10.1088/0004-637X/754/2/132)
- Tappe, A., Rho, J., & Reach, W. T. 2006, *ApJ*, 653, 267, doi: [10.1086/508741](https://doi.org/10.1086/508741)
- Tatematsu, K., Fukui, Y., Iwata, T., Seward, F. D., & Nakano, M. 1990, *ApJ*, 351, 157, doi: [10.1086/168452](https://doi.org/10.1086/168452)
- Tatematsu, K., Fukui, Y., Nakano, M., et al. 1987, *A&A*, 184, 279
- Temim, T., & Dwek, E. 2013, *ApJ*, 774, 8, doi: [10.1088/0004-637X/774/1/8](https://doi.org/10.1088/0004-637X/774/1/8)
- Temim, T., Slane, P., Reynolds, S. P., Raymond, J. C., & Borkowski, K. J. 2010, *ApJ*, 710, 309, doi: [10.1088/0004-637X/710/1/309](https://doi.org/10.1088/0004-637X/710/1/309)
- Temim, T., Slane, P., Sukhbold, T., et al. 2019, *ApJL*, 878, L19, doi: [10.3847/2041-8213/ab237c](https://doi.org/10.3847/2041-8213/ab237c)
- Tian, W. W., & Leahy, D. A. 2008, *MNRAS*, 391, L54, doi: [10.1111/j.1745-3933.2008.00557.x](https://doi.org/10.1111/j.1745-3933.2008.00557.x)
- Todini, P., & Ferrara, A. 2001, *MNRAS*, 325, 726, doi: [10.1046/j.1365-8711.2001.04486.x](https://doi.org/10.1046/j.1365-8711.2001.04486.x)
- Trimble, V. 1968, *AJ*, 73, 535, doi: [10.1086/110658](https://doi.org/10.1086/110658)
- Troja, E., Bocchino, F., & Reale, F. 2006, *ApJ*, 649, 258, doi: [10.1086/506378](https://doi.org/10.1086/506378)
- van Dishoeck, E. F., Jansen, D. J., & Phillips, T. G. 1993, *A&A*, 279, 541
- Velázquez, P. F., Dubner, G. M., Goss, W. M., & Green, A. J. 2002, *AJ*, 124, 2145, doi: [10.1086/342936](https://doi.org/10.1086/342936)
- Vermeij, R., Damour, F., van der Hulst, J. M., & Baluteau, J. P. 2002, *A&A*, 390, 649, doi: [10.1051/0004-6361:20020424](https://doi.org/10.1051/0004-6361:20020424)
- Vermeij, R., & van der Hulst, J. M. 2002, *A&A*, 391, 1081, doi: [10.1051/0004-6361:20020864](https://doi.org/10.1051/0004-6361:20020864)
- Williams, B. J., Borkowski, K. J., Reynolds, S. P., et al. 2008, *ApJ*, 687, 1054, doi: [10.1086/592139](https://doi.org/10.1086/592139)
- Wootten, A. 1981, *ApJ*, 245, 105, doi: [10.1086/158790](https://doi.org/10.1086/158790)
- Yuan, Y., & Neufeld, D. A. 2011, *ApJ*, 726, 76, doi: [10.1088/0004-637X/726/2/76](https://doi.org/10.1088/0004-637X/726/2/76)
- Zhou, P., Chen, Y., Safi-Harb, S., et al. 2016, *ApJ*, 831, 192, doi: [10.3847/0004-637X/831/2/192](https://doi.org/10.3847/0004-637X/831/2/192)
- Zhou, P., Vink, J., Safi-Harb, S., & Miceli, M. 2019, *A&A*, 629, A51, doi: [10.1051/0004-6361/201936002](https://doi.org/10.1051/0004-6361/201936002)